TECHNISCHE
UNIVERSITÄT
WIEN
Vienna University of Technology

INSTITUTE OF
LIGHTWEIGHT DESIGN AND
STRUCTURAL BIOMECHANICS

Diplomarbeit

Prediction of energy dissipation due to material nonlinearities and its application to textile composites

ausgeführt zum Zwecke der Erlangung
des akademischen Grades eines Diplom-Ingenieurs
unter der Leitung von

Associate Prof. Dipl.-Ing. Dr.techn. Heinz Pettermann
Dipl.-Ing. Dr.techn. Jakob Gager

Institut für Leichtbau und Struktur-Biomechanik (E317)

eingereicht an der Technischen Universität Wien
Fakultät für Maschinenwesen und Betriebswissenschaften

von

Martin Schwab, BSc.
0825772
Eduard Pichlerstr. 3
3860 Heidenreichstein

Wien, am 19. November 2013 Martin Schwab

Acknowledgements

First of all, I want to thank my thesis advisors, Prof. Heinz Pettermann and Jakob Gager, for their valuable support during all stages of this work. Their positive attitude always encouraged me and the numerous discussions helped me to reflect critically and develop new ideas.

The funding of the Polymer Competence Center Leoben (PCCL, Austria) within the framework of the COMET-program of the Austrian Ministry of Traffic, Innovation and Technology and the State Governments of Styria and Upper Austria is greatfully acknowledged.

I want to thank my friends for inspiring and motivating each other, but also for providing the necessary compensation to calm down. Finally, I want to thank my family, without whose support none of this would have been possible.

Inhaltsverzeichnis

Zusammenfassung

Faserverbundwerkstoffe bedienen sich, nicht zuletzt aufgrund ihrer hervorragenden gewichtsspezifischen Eigenschaften, immer größer werdender Popularität in vielen Bereichen des Maschinenbaus. Um ihr volles Potential ausschöpfen zu können, ist die Vorhersage des nichtlinearen Verhaltens von Strukturen aus diesen Materialen unabdingbar, was jedoch sehr hohen Rechenaufwand mit sich bringt und in der Praxis bislang kaum durchführbar ist. Das Ziel dieser Arbeit ist es, die Vorhersagemöglichkeiten linear elastischer Analysen großer Bauteile durch Berücksichtigung von Informationen zu nichtlinearen Effekten, gewonnen über Simulationen auf kleineren Längenskalen, zu erweitern. Diese Vorgehensweise reduziert den Rechenaufwand auf ein praktikables Maß. Die vorgestellte Methode ist universell anwendbar, wobei der Fokus dieser Arbeit auf die Anwendung auf Textillaminate gerichtet ist.

Es wird eine Modellierungsstrategie zur Simulation des nichtlinearen Verhaltens von Textillaminaten auf kleinen Längenskalen über sogenannte Einheitszellen beschrieben und mehrere Konstitutivgesetze, welche Schädigung und Plastizität modellieren, vorgestellt. Eine Methodologie zur Kombination der aufgezeichneten Nichtlinearitäten mit linear elastischen Berechnungen wird eingeführt, wobei zuerst die Erzeugung einer Datenbank, welche die nichtlinearen Einheitszellenantworten zu einer Verteilung von ebenen Spannungszuständen enthält, erklärt wird und dann die Prozedur zur Bewertung linear elastisch berechneter Zustände hinsichtlich auftretender Nichtlinearitäten vorgestellt wird. Die Generierung einer derartigen Datenbank wird am Beispiel eines biaxialen Gewebes mit Körperbindung demonstriert und die beschriebene Prozedur wird anhand eines U-Profils mit veränderlicher Flanschhöhe in einem 4-Punkt Biegeversuch präsentiert. Die vorgestellte Methodik zeigt gute Anwendbarkeit bis zum leicht nichtlinearen Bereich und erlaubt verbesserte Aussagen über eventuell vorhandene Festigkeitsreserven wodurch eine detailliertere Auslegung von Faserverbundbauteilen ermöglicht werden soll.

Abstract

Fibre reinforced composites are becoming increasingly popular in almost every field of engineering, not least due to their favourable weight specific properties. In order to exploit the full potential of these materials, a reliable prediction of the nonlinear response of structural components is inevitable, which, however, claims huge computational effort and is, in practice, hardly feasible up to now. The aim of this work is to extend the predictional capabilities of large-scale linear elastic analyses by combining them with information on nonlinear effects gained through analyses at smaller length scales, thus reducing the computational demands to a practicable extent. The presented approach is universally applicable, while this work concentrates on the application on textile composites.

A modelling strategy for capturing the nonlinear mechanical behaviour of textile composites at small length scales is described on the basis of a so-called unit cell approach and several constitutive models for simulating damage and plasticity are presented. A methodology for combining the monitored nonlinearities at small length scales with the results of large-scale linear elastic analyses is introduced. In a first step, a database of nonlinear unit cell responses to a distribution of plane stress states is generated and, second, a procedure for assessing linear elastically computed states regarding occurring nonlinearities is proposed. The generation of such a database is demonstrated by the example of a 2/2 twill weave. In this context, also the influence of the application of different constitutive models on the evolution of dissipated energies is investigated. The assessment of nonlinearities in large components is presented by the example of a U-section beam with variable flange height in a four point bending test set-up consisting of several layers of ±30° twill braidings. The proposed methodology shows good applicability up to the slightly nonlinear regime thus giving information beyond the linear elastic limit and allows for a more detailed investigation of the mechanical performance of composites.

Chapter 1

Introduction

1.1 General Remarks

During the past years the application of fibre reinforced polymers (FRP) has increased significantly in almost every field of engineering. Due to their favourable weight specific properties, namely high specific stiffness and strength, they are particularly advantageous in lightweight components. Therefore especially aerospace and automotive industry aim at exploiting the potential of FRPs more and more. To this end, it is necessary to reliably predict the structural response of components consisting of FRPs up to the nonlinear regime which, however, is still subject to research nowadays. Although computational methods and performance have improved, mostly linear analyses are used for stiffness and strength predictions thus limiting the range of application. The aim of this work is to contribute to the development of computational models which allow for gaining knowledge of the structural response beyond the linear limit, thus giving information about strength reserve and helping to better identify critical spots in a construction.

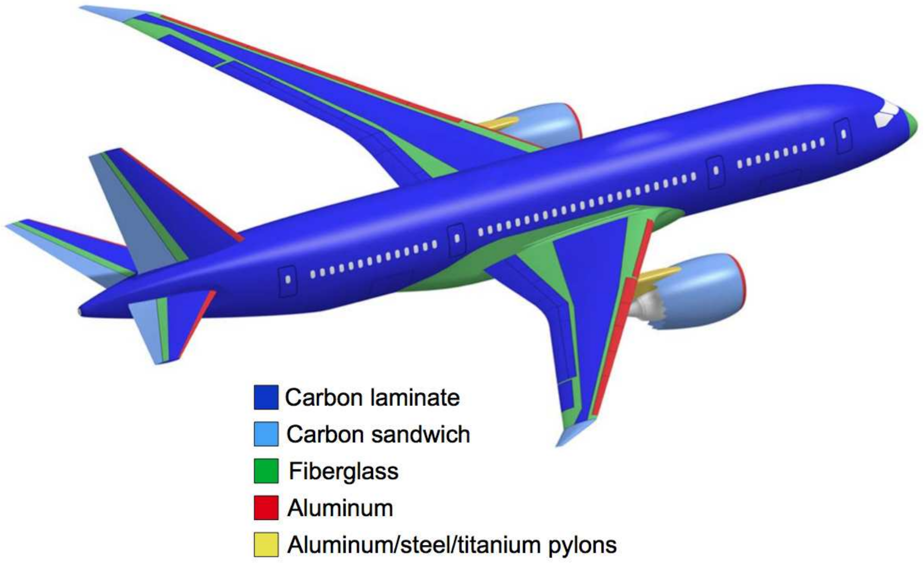

Figure 1.1: Materials usage in a Boeing 787 Dreamliner. [22]

In order to recall the importance of FRPs the makeup of the Boeing 787 Dreamliner is shown in Fig. 1.1 as an example from aerospace industry. As can be seen composite materials are used in every major part, thus, increasing the amount of composites to 50 percent of the total mass. The following sections give a short overview of the different types of FRPs and their failure behaviour. Furthermore typical analysis methods are outlined in order to give some basic knowledge in the field of composites engineering. The textbook [32] may be useful in order to get more detailed information on the structure, properties and also production processes of FRPs.

1.2 Scope of the Present Work

The prediction of all relevant nonlinear mechanisms in large composite components leads to vast computational demands and is, in practice, hardly feasible up to now.

The aim of this work is to extend the predictional capabilities of large-scale linear elastic analyses by combining them with information on nonlinear effects gained through analyses at smaller length scales, thus reducing the computational effort to a practicable extent. The presented approach is universally applicable, however, this work concentrates on the application on textile composites.

First, a general classification of composites with focus on fibre reinforced polymers is conducted and a short summary of their failure behaviour is given. Additionally, remarks on first ply failure analysis and progressive damage modelling are listed. After these general informations on the field of composites engineering are stated, the utilized modelling strategy for textile composites is described, where a so-called unit cell approach is used to model the entire nonlinear behaviour of a textile ply. After different constitutive models for simulating damage and plasticity are described a method for monitoring the occurring nonlinearities is presented.

Chapter 4 introduces a two step methodology for combining the monitored nonlinearities at small length scales with the results of large-scale linear elastic analyses. Therefore, in a first step, a database of nonlinear unit cell responses to a distribution of plane stress states is generated, where each state is computed along radial stress and radial strain paths in order to account for the influence of non-proportional loading in the nonlinear regime. Second, a procedure for mapping linear to nonlinear states is proposed and the utilization of the generated database in order to assess linear elastically computed states regarding occurring nonlinearities is explained.

The example of a twill weave is used to demonstrate the generation of such a database and levels of dissipated energies corresponding to different nonlinear mechanisms are illustrated as envelopes in plane stress space. In this context, also the influence of the application of different constitutive models on the evolution of dissipated energies is investigated. The assessment of nonlinearities in large components is presented by the example of a U-section beam with variable flange height in a four point bending test set-up consisting of several layers of ±30° twill braidings. In the end, a short summary of the work is given and conclusions on the presented methodology are stated.

Chapter 2

Fibre Reinforced Composites

2.1 Classification of Composites

In the most general sense, composites are materials consisting of two or more different constituents with clearly recognizable interfaces. The basic advantage of these materials lies in the combination itself, which allows for the design of specific material properties customized for particular load cases. Usually, such a composite consists of two phases (constituents), where one of them is characterized by high stiffness and strength (reinforcement) thus being responsible for carrying the load and the other one ensures the cohesion of the compound (matrix). A classification of the various types can be conducted either by the matrix material or the type of the reinforcement. Proceeding with the latter, particulate composites, discontinuous fibre reinforced composites and continuous fibre reinforced composites are distinguished. Since this work deals with continuous fibre reinforced composites with a polymer matrix, continuous fibre reinforced polymers (CFRPs), the other two categories are not further discussed.

In CFRPs very thin fibres, mostly glass or carbon fibres, are combined to form linear strands which are either directly used to form a component or further processed to result in some 2 dimensional preform. The strands differ in the number of fibres combined and their twist and are known as rovings, tows or yarns, to name some of them. Often, lightweight structures contain thin-walled shell structures where the use of planar preforms is beneficial. In this case the fibres are processed to weaves, braids, knitted fabrics or unidirectional non-woven arrangements (tapes) depending on the field of application, compare Fig. 2.1. The waviness of the fibres additionally influences the material properties of the compound, meaning that a higher amount of fibre curvature leads to additional stresses in the fibres, which results in lower stiffness and strength of the final material. However, the waviness adds more resistance against shear distortion and the unhardened preform is more stable and thus easier to handle in processing. Depending on the production method, the fibre material already combined with

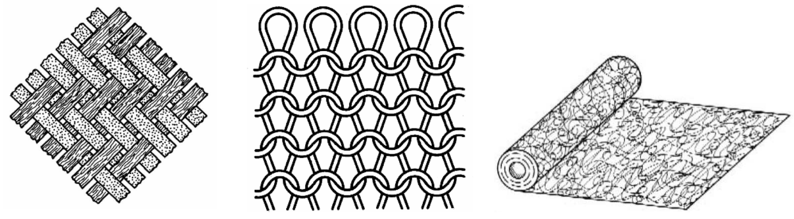

(a) weave (b) knitted fabric (c) fleece

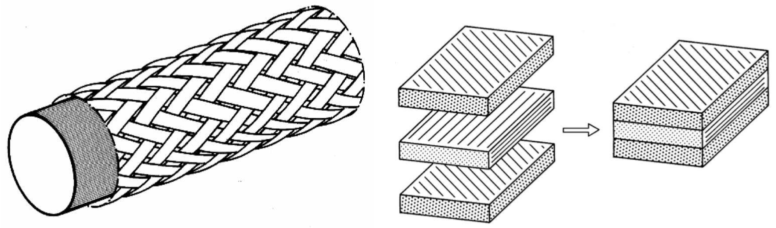

(d) braid (e) laminate

Figure 2.1: (a) to (d): Different fibre preforms. (e) Example of a laminate consisting of 3 unidirectional layers with different orientations. [32]

an amount of matrix material, for example epoxy, which is partially cured to allow easy handling. Those pre-impregnated fibres (pre-pregs), mostly weaves or unidirectional tapes, are very popular in aerospace applications. In order to form a component, several layers (lamina) of those pre-processed arrangements are combined (laminate), often with varying fibre orientation as optimization for the most relevant load cases.

Weaves are the most common fibre arrangements in lightweight structures where more than one fibre orientation is required. Their drapability, surface smoothness and stability are mainly controlled by the weave style. Usually they are represented by two perpendicular oriented fibre directions called weft and warp. In the case of the simplest one, the plain weave, each warp fibre passes one weft fibre on top and the following one on the bottom continued alternately, compare Fig. 2.2 (a). However, the high degree of fibre waviness in such plain weaves causes poorer drapability and decreases fatigue strength and other mechanical properties, cf. [32]. Therefore other weave styles with reduced waviness, like twill weaves or satin weaves, are used for highly loaded components up to unidirectional weaves, where 90 percent of the fibres are oriented in the same direction (warp fibres) and the weft fibres are just used to keep their position, compare Fig. 2.2 (b) to (d).

Braided fabrics are more complex in production than weaves and also limited in dimensions due to the size of the braiding machine. Nevertheless, this technique is often used to form axi-symmetric bodies like tubes or pressure cylinders. The fibre orientation is adjustable from 15° to 85° with respect to the axial direction.

Unidirectional tapes are quite similar to unidirectional weaves, however, the positioning of the fibres is ensured by stitching in this case. Fleeces have rather poor mechanical properties and are primarily used as the outermost layer of a composite to generate a smooth surface and to improve the impact strength and

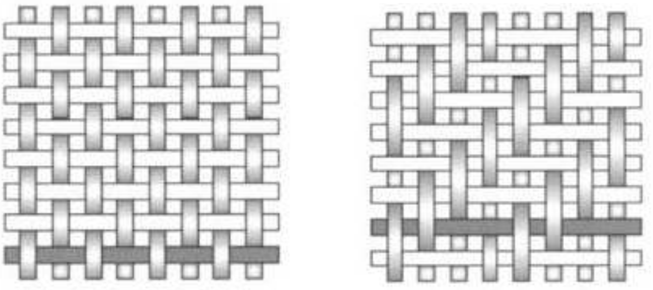

(a) plain weave (b) twill weave

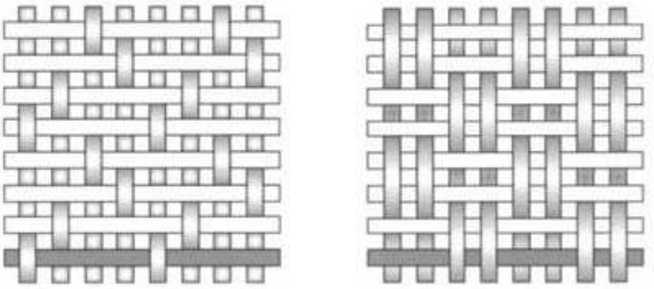

(c) satin weave (d) basket weave

Figure 2.2: Different weave styles. [4]

resistance to weather. Knitted fabrics feature the highest flexibility and the ability to wrinkle-free cover 3D curved shapes with the disadvantage of lower mechanical properties, cf. [32].

Finally, it shall be stated that the mechanical response of the composites described above usually varies depending on the load orientation, thus being non-isotropic. In most cases the material symmetry is orthotropic or transversally isotropic but the final properties depend on the ones of each layer and the sequence of the layers in the laminate. Additionally those materials are obviously inhomogeneous. In order to properly assess the loading state and strength of a CFRP component, knowledge of the possible failure mechanisms is inevitable.

2.2 Failure-Behaviour of Fibre Reinforced Polymers

Besides global failure of the structure due to huge deformations or global instability there are several mechanisms arising from internal material failure at the micro- or mesoscale. Those can be distinguished between failure in a single layer (ply) of the laminate or in the interface between the plies (delamination). The following remarks describe the failure behaviour of unidirectional fibre reinforced polymers and are based on [32] and [33] but the interested reader my also be referred to [25], [27] and [17].

Ply failure comprises cracking of the fibres, the matrix and also failure of the interface between the fibres and the matrix. Since the mechanical response of FRPs is direction dependent, the occurring failure modes also show direction dependence. Thus, uniaxial tensile loads in fibre direction may lead to fibre cracking, fibre pullout, failure due to shear stresses in the fibre-matrix interface or debonding of fibres and matrix. The actually dominating mechanism is depending on the materials, the fibre volume fraction and of course potential shortcomings in the production process. Considering uniaxial compressive loading in fibre direction several other mechanisms may occur. In this context, transverse tensile strains caused by the different poisson ratios of fibre and matrix material can lead to transversal cracks in the matrix (transverse splitting) and also in the interface (debonding). Additionally, instability phenomena can arise since the fibres act like thin columns elastically embedded in the matrix. The corresponding failure mode is called fibre microbuckling where adjacent fibres either buckle independently (extensional mode) when the distance between them is high enough or in parallel (shear mode). Another instability mechanism leads to the formation of so-called kinkbands and is known as fibre kinking. In this case several adjacent fibres kink in the same direction often starting from regions with small imperfections. Uniaxial tensile loads in transversal direction cause stress concentrations in the matrix due to the different Young's modulus of the fibre material which obstructs the matrix deformation. This reduces the tensile strength compared to the one of the plain matrix material. The occurring mechanisms are transverse matrix cracking, debonding and also fibre splitting. The corresponding compressive loading results in matrix shear failure, debonding or fibre splitting where a combination of all modes can occur along shear planes. Typically, these effects are accompanied by plasticity effects. The last generic load case which shall be discussed is in-plane shear. Here, the relevant failure mode depends on the strength of the fibre-matrix interface and is either characterized by matrix shear failure if the interface is strong or debonding in the opposite case, where both modes may be accompanied by unrecoverable strain accumulation. Additionally, also a combination of both is possible.

Delamination describes the separation of adjacent layers of a laminate due to interlaminar normal or shear tractions, respectively, and can occur inside the laminate but also in the vicinity of free edges. Delamination inside a laminate can be caused by several effects, some of them are impact damage, fatigue loading, moisture or structural discontinuities. Free edge delamination, on the other hand, occurs due to different material properties of adjacent plies leading to a tri-axial stress state in those regions. The range of influence of this so-called free edge effect is about the same size as the laminate thickness.

Considering a laminate under some general stress state which is proportionally increased, at some point failure will occur at the weakest point of the laminate (first ply failure). If the load is further increased stress redistribution occurs and more regions are going to be damaged but the ultimate strength may not be reached yet. The point where the whole laminate fails is called last ply failure.

2.2.1 First Ply Failure Analysis

In order to evaluate stresses and strains in a laminate elastostatic methods are applied. According to the historical progress, most of those methods have been developed for the application on UD laminates, as for example the classical lamination theory which can be reviewed in [15]. Here, the global strains of the laminate are calculated and evaluated for each ply followed by a transformation to the respective local coordinate system. Now the local constitutive equations are solved which finally yields the occurring stresses in each ply.

However, a strength analysis does not only require knowledge of the actual acting stresses but also of the maximum allowable ones. Those are, in most cases, determined for simple load cases thus necessitating the formulation of a criterion to differentiate complex stress states leading to failure from allowable states. Such a criterion,

$$F(\sigma_{ij}, R_{kl}^{t,c}) \lesseqgtr 1, \tag{2.1}$$

represented in form of a general function F of the stress tensor σ_{ij} and the material strengths $R_{kl}^{t,c}$ for tension t and compression c identifies stress states causing first identifiable damage of the ply (first ply failure).

Usually these failure criteria are applied at the ply level with reference to the ply coordinate system, where a value of the function in Eq. (2.1) smaller than 1 means that the currently acting load can be withstood without failure while a value larger than 1 marks states where failure has already occurred. Assuming linear elastic material behaviour, a scalar factor λ representing the value, the

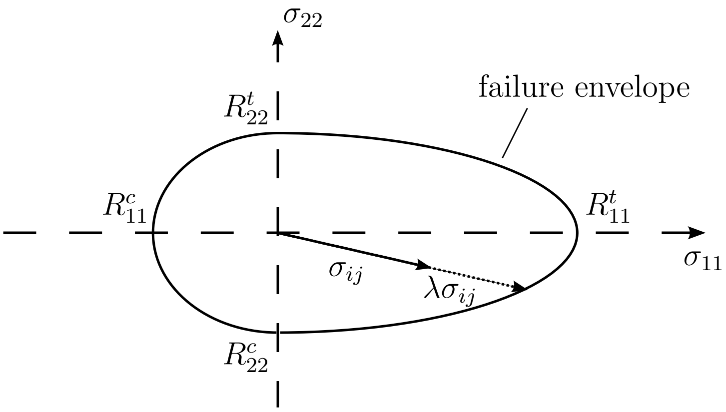

Figure 2.3: Visualization of a failure criterion as an envelope of allowable conditions for a biaxial stress state.

current stress tensor σ_{ij} has to be multiplied with in order to reach the limit state ($F = 1$) can be introduced, thus representing the safety factor. Additionally to the mathematical formulation above, failure criteria can also be visualized as failure surfaces or failure envelopes in stress space, compare Fig. 2.3. The failure envelope itself differs according to the actual criterion used and represents all stress states which lead to first ply failure (FPF) upon further load increase.

Basically, there are two types of failure criteria. They can either be a mathematical construction formulated in a way which eases the adaption to fit experimental data, like Tsai-Hill or Tsai-Wu (cf. [15], [16]), or they are motivated from physical failure mechanisms. A popular representative of the latter is the criterion developed by Puck, cf. [25], [27], [26], and also the one from Hashin [12]. The World-Wide Failure Exercise [14] aims at validating the predictive capabilities of several failure criteria and reveals that the Puck criterion ranks among the most accurate ones. Although a FPF analysis is straightforward in its use for initial component design and has only low computational demands it gives no information about what happens after reaching the failure condition in a single ply of the laminate. Thus, it is not possible to estimate the severeness of the current state and no predication of the strength reserve can be given. In order to do so, the application of continuum damage mechanics is necessary.

2.2.2 Progressive damage modelling

The purpose of progressive damage modelling lies in the coverage of the mechanical behaviour of a laminate after a failure condition, as described above, has been met at a certain point in one ply. In order to account for the influence of propagating damage, two basically different approaches are possible. On the one hand, concepts from fracture mechanics can be utilized for evaluating crack initiations and propagations which give rise to the amount of damage and also the associated stress redistribution. However, the underlying computational model needs to resolve stresses and strains at a microscopic level which increases the complexity and restricts their application to small domains.

Another approach is known as continuum damage mechanics and is applied at larger length scales, such as the mesoscopic or even the macroscopic level. Here, the inhomogeneous material, typically a single ply, is assumed to be homogeneous and the material properties of the constituents are replaced by effective material properties. Additionally, damage is also assumed to be evenly distributed and causes stiffness degradation of the affected domain. In this way load redistribution can be modelled, although damage modes of adjacent domains do not interact directly. The benefit of this method reflects in the fact that the stress and strain state only needs to be known at, for example, the ply-level which reduces the computational effort essentially. A simple way to account for the stiffness degradation is the use of a scalar damage variable d, as proposed in [28].

$$E^{dam} = (1 - d)E^{init}, \tag{2.2}$$

In the uniaxial case, its impact on the Young's modulus can be described according to Eq. (2.2), where the Young's modulus of the undamaged material E^{init} is reduced according to the present amount of damage d in order to obtain the Young's modulus of the damaged configuration E^{dam}. This approach can also be generalized for multi-axial stress states resulting in tensorial equations and several damage variables. However, the formulation of a constitutive law requires the definition of the evolution of these damage variables and their effect on the degradation of material properties. One methodology is based on FPF theories and tries to describe propagating damage in a phenomenological way according to experimental data. Although relations set up in this way are quite straightforward, they are not necessarily physically consistent, meaning that these constitutive laws do not fulfil conservation equations. Therefore most continuum damage models incorporate thermodynamical considerations to overcome this disadvantage. Using continuum mechanics to model damage comprises the assumption that the length scale of the cracks must be considerably smaller than the characteristic length scale of the continuum, e.g. the ply thickness, which doesn't always hold true. All the above mentioned approaches lead to nonlinearities in the material response and aim at reproducing the real material behaviour. However, continued loading and unloading tests of specimens have shown that unrecoverable strains can occur, thus giving rise to include plasticity in more sophisticated models as well. A good overview of the development of damage mechanics and the available models is given in [8], which also describes a constitutive model used in this work. It will be discussed in more detail in the following chapters together with the simpler one from [18], which is implemented in the commercial finite element code Abaqus/Standard v6.12 (*Dassault Systemes Simulia Corp., Providence, RI, USA*).

Chapter 3

Modelling Textile Composites

The structure of a composite laminate can be divided into several length scales which have to be accounted for in the corresponding model. Typically, three length scales are distinguished, namely the macroscale, mesoscale and mircoscale. A characteristic length of the component is then denoted as macroscale while, for example, laminate or ply level represents the mesoscale in a composite. The microscale describes the length scale of the inhomogeneities like the fibre diameters or distances between them. This hierarchy can be seen in Fig. 3.1, where a part of an aeroplane's wing consists of textile laminates. In order to describe the mechanical properties of such inhomogeneous materials, micromechanical approaches can be used beneficially when the length scales are sufficiently far apart. Then it can be assumed that the stress and strain fields at smaller length scales (microfields) influence the macroscopic behaviour only via their volume averages and the macroscopic fields are seen as constant from a microscopic point of view. Accordingly, once the microfields are determined they are averaged over a specified volume in order to get the macroscopic response which agrees with the overall material properties if the averaging volume contains all necessary information. When

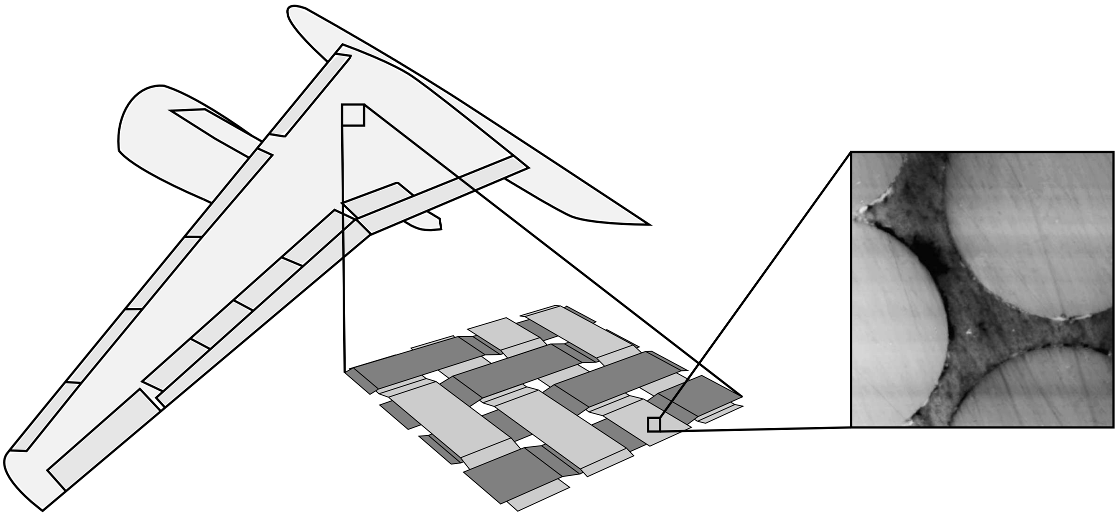

Figure 3.1: Different lengths scales in a component consisting of composite laminates. The structure itself represents the macroscale (left, based on [24]). When zooming in, the plies of the laminate, built from several tows, get visible and characterize the mesoscale in this case (middle). Another step closer, single fibres in a ply are recognizable denoting the microscale (right, [8]).

this is the case, a representative volume element (RVE) is chosen. The described procedure is known as homogenization, whereas the opposite way is termed localization. Basically, two groups of micromechanical methods can be distinguished, where some describe the microgeometries based on statistical information, like mean field approaches (MFA) or bounding methods, and others try to describe discrete microstructures. The following section describes the general geometric modelling of a composite's microstructure by applying a method of the latter group, a periodic microfield approach (PMA), and is based on [23] together with [3], which represents a good summary of micromechanical methods. In the context of this work a PMA is utilized to model the mesoscale geometry of a textile ply in order to predict the entire nonlinear response at this length scale. The second part of this chapter describes the applied material models at the mesoscale thus giving an entire overview of the modelling strategy.

3.1 Unit Cell Approach

The characteristics of inhomogeneous materials featuring periodic arrangements of constituents, as typical for textile composites, can be studied conveniently using PMAs. The most common method divides the meso/mircostructure into periodically repeating unit cells where the analysis of just one of them is sufficient for covering the entire material behaviour. However, it shall be noted that this approach considers the investigated domain to be infinitely extended by translations of the unit cell along the axes of periodicity which has to be taken into account when applying the results to the macrostructure. The analyses in this work utilize a unit cell model in combination with the finite element method for the numerical evaluation.

3.1.1 Periodicity

Periodic materials can be categorized according to their number of axes of periodicity. The most general type exhibits three axes of periodicity and is termed spatially periodic whereas two axes of periodicity denote plane periodic arrangements which are discussed in this section.

According to [2] and [23] a periodic medium can be described by independent vectors of periodicity $\underline{\boldsymbol{p}}^k$ where $k = A, B$ in the case of plane periodicity.

$$\begin{aligned} \underline{\boldsymbol{p}}^A &= l_1 \ \underline{\boldsymbol{e}}^1 \\ \underline{\boldsymbol{p}}^B &= d_2 \ \underline{\boldsymbol{e}}^1 + l_2 \ \underline{\boldsymbol{e}}^2 \end{aligned} \tag{3.1}$$

These vectors are in general not necessarily perpendicular to each other, as illustrated in Fig. 3.2, and are defined corresponding to Eq. (3.1) where l_1 and l_2 are

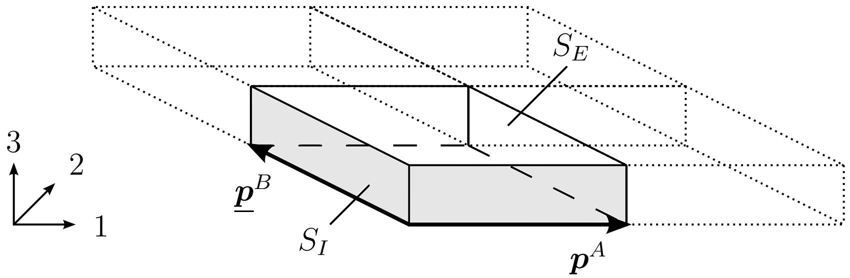

Figure 3.2: Plane periodic arrangement with periodicity vectors $\underline{\boldsymbol{p}}^A$ and $\underline{\boldsymbol{p}}^B$.

the dimensions of the unit cell and d_2 represents the offset in $\underline{\boldsymbol{e}}^2$-direction, meaning that $d_2 = 0$ results in perpendicular periodicity vectors. The geometrical and mechanical properties of a point $\underline{\boldsymbol{x}}_1$ of the periodic material are identical to the ones of any point $\underline{\boldsymbol{x}}_2$ if the vector $\underline{\boldsymbol{x}}_2 - \underline{\boldsymbol{x}}_1$ is a linear combination of integral multiples of $\underline{\boldsymbol{p}}^A$ and $\underline{\boldsymbol{p}}^B$. The vector $\underline{\boldsymbol{t}}$ in Eq. (3.2) represents such a linear combination, where m_A and m_B are integers.

$$\underline{\boldsymbol{t}} = m_A \ \underline{\boldsymbol{p}}^A + m_B \ \underline{\boldsymbol{p}}^B \tag{3.2}$$

Considering a function $\mathcal{F}(\underline{\boldsymbol{x}})$ describing the spatial variation of an arbitrary material property or state the above statement can be expressed as

$$\mathcal{F}(\underline{\boldsymbol{x}}) = \mathcal{F}(\underline{\boldsymbol{x}} + \underline{\boldsymbol{t}}), \tag{3.3}$$

allowing the investigations to be conducted on the domain of a single unit cell without loss of information. The shape of the unit cell is determined by the material's topology, however often several arrangements are possible as illustrated in Fig. 3.3. Additionally to the spatial description of periodic properties the boundary conditions along the borders of the unit cell have to be defined accordingly. The faces S_I, cf. Fig. 3.2, therefore have to imitate an infinite extension of the domain, meaning that reaching the boundary on one side of the unit cell corresponds to start from the opposite side again. The respective mechanical requirements are

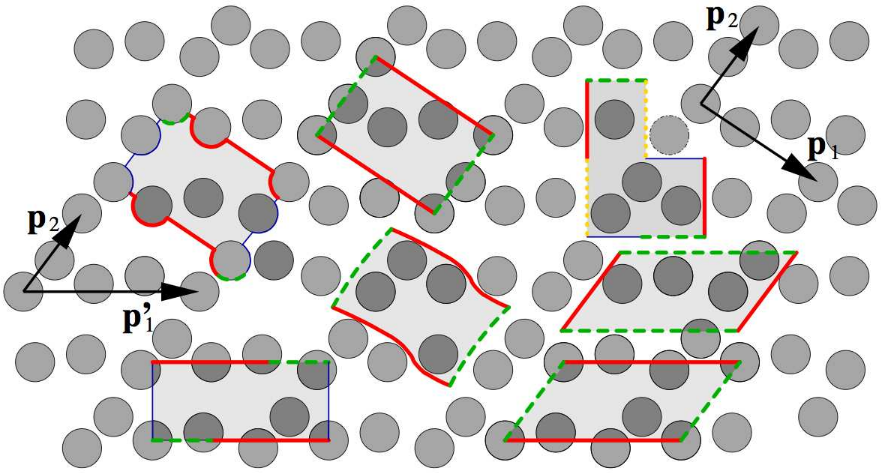

Figure 3.3: Possible minimum-size unit cell shapes for a two dimensional periodic arrangement of inhomogeneities with periodicity vectors $\underline{\boldsymbol{p}}_1$ and $\underline{\boldsymbol{p}}_2$. Paired faces are marked by identical line styles. [3]

the continuity of the traction vector T_i and the compatibility of deformations along S_I, where the last condition makes sure that neither overlapping nor separation occurs. The first condition reads as follows (cf. [23], [2])

$$T_i^+ = -T_i^- \qquad n_i^+ = -n_i^-, \tag{3.4}$$

where the superscripts + and − denote opposite sides and n_i represents the normal vector. The requirement of compatible deformations leads to a periodic strain field and can be expressed in terms of displacements for shell-like planar media according to Eq. (3.5) (cf. [23]), where $\mathcal{E}_{ij}$ is the mean (macroscopic) strain tensor, χ_{ij} the mean (macroscopic) curvature change tensor (cf. shell theory) and $u_i^P(\underline{\boldsymbol{x}})$ denotes periodically varying microscopic fluctuations of the displacement field.

$$\begin{aligned} u_i(\underline{\boldsymbol{x}}) &= \mathcal{E}_{ij}\ x_j - \chi_{ij}\ x_j\ x_3 + u_i^P(\underline{\boldsymbol{x}}) \qquad i,j = 1,2 \\ u_3(\underline{\boldsymbol{x}}) &= \frac{1}{2}\ \chi_{mn}\ x_m\ x_n + u_3^P(\underline{\boldsymbol{x}}) \qquad m,n = 1,2 \end{aligned} \tag{3.5}$$

The upper and lower faces of the unit cell, S_E, on the other hand, represent a "true" external boundary in the plane periodic case and are therefore stress-free, thus giving rise to assume plane stress conditions for the further analysis. The above described conditions can be summarized under the term "plane periodic boundary conditions".

3.1.2 Homogenization of Stresses and Strains

The above described unit cell model is going to be incorporated into a finite element model. However, this approach requires some special techniques in comparison to standard FEM applications. Besides the periodic couplings explained above, the question arises of how macroscopic (far field) stress and strain states are applied as boundary conditions to the unit cell since the variations caused by the microstructure are not known a priori. On the other hand, the computed microfields include these variations whereas mostly mean (macroscopic) fields are of interest for evaluating material properties.

According to [23] it can be shown that the mean strain and stress tensors $\mathcal{E}_{ij}$ and Σ_{ij} are identical to the volume average of the corresponding microfields $\varepsilon_{ij}(\underline{\boldsymbol{x}})$ and $\sigma_{ij}(\underline{\boldsymbol{x}})$ over the unit cell volume, cf. Eq. (3.6).

$$\mathcal{E}_{ij} = \frac{1}{V}\int\limits_V \varepsilon_{ij}(\underline{\boldsymbol{x}})dV \qquad \Sigma_{ij} = \frac{1}{V}\int\limits_V \sigma_{ij}(\underline{\boldsymbol{x}})dV \tag{3.6}$$

Although these relations can be used for homogenization, they are not useful for applying suitable boundary conditions arising from far field loads. Therefore the "method of macroscopic degrees of freedom", see [21], is utilized for the evaluation of microfields and application of loads. In order to control the analysis, concentrated nodal forces or displacements are applied at master nodes, which in turn

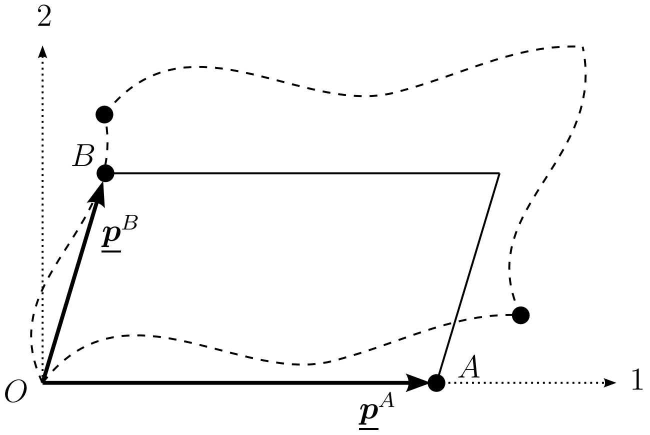

Figure 3.4: Example of a 2D unit cell with periodicity vectors $\underline{\boldsymbol{p}}^A$ and $\underline{\boldsymbol{p}}^B$ and the corresponding master nodes A and B. A possible deformed state is shown as dashed lines. The origin O of the 1,2 coordinate system is connected to the lower left corner of the unit cell.

govern the unit cell's response and are additionally used for evaluating the mean stress and strain tensors. The homogenized strain tensor $\mathcal{E}_{ij}$ follows directly from Eq. (3.5) with $x_3 = 0$ and the displacements for two corresponding points can then be written as

$$\begin{aligned} u_i(\underline{\boldsymbol{x}}) &= \mathcal{E}_{ij} x_j + u_i^P(\underline{\boldsymbol{x}}) \\ u_i(\underline{\boldsymbol{x}} + \underline{\boldsymbol{t}}) &= \mathcal{E}_{ij}(x_j + t_j) + u_i^P(\underline{\boldsymbol{x}}) \end{aligned} \tag{3.7}$$

Considering the situation illustrated in Fig. 3.4, where $\underline{\boldsymbol{x}} = \underline{\boldsymbol{0}}$ and $u_i(\underline{\boldsymbol{0}}) = \underline{\boldsymbol{0}}$, it follows that $\underline{\boldsymbol{t}} = \underline{\boldsymbol{p}}^k$. Taking the difference of the two relations in Eq. (3.7) and keeping in mind that the periodically varying fluctuations of the displacement field are equal $u_i^P(\underline{\boldsymbol{0}}) = u_i^P(\underline{\boldsymbol{p}}^k)$ leads to

$$u_i(\underline{\boldsymbol{p}}^k) = u_i^k = \mathcal{E}_{ij} p_j^k \qquad k = A, B \tag{3.8}$$

where u_i^k indicates the master node displacements. The periodicity vectors $\underline{\boldsymbol{p}}^A$ and $\underline{\boldsymbol{p}}^B$ represent the undeformed state and are mapped onto the corresponding displacements via the mean strain tensor $\mathcal{E}_{ij}$. More precisely, $\mathcal{E}_{ij}$ corresponds to the displacement gradient tensor according to finite strain theory and is just identical to the linear strain tensor in the case of small deformations. This aspect will be discussed in the following section. Eq. (3.8) can also be written in matrix form as

$$\underbrace{\begin{pmatrix} u_1^A & u_1^B \\ u_2^A & u_2^B \end{pmatrix}}_{\underline{\underline{\boldsymbol{U}}}} = \underbrace{\begin{pmatrix} \mathcal{E}_{11} & \mathcal{E}_{12} \\ \mathcal{E}_{21} & \mathcal{E}_{22} \end{pmatrix}}_{\underline{\underline{\boldsymbol{\mathcal{E}}}}} \cdot \underbrace{\begin{pmatrix} p_1^A & p_1^B \\ p_2^A & p_2^B \end{pmatrix}}_{\underline{\underline{\boldsymbol{P}}}} \tag{3.9}$$

and is used for evaluating the boundary conditions in a strain controlled analysis. The superscripts indicate the respective master node whereas the subscripts correspond to the coordinate system in Fig. 3.4. In order to gain the homogenized strains as the result of a stress controlled analysis, Eq. (3.9) can be transformed as follows.

$$\underline{\underline{\boldsymbol{\mathcal{E}}}} = \underline{\underline{\boldsymbol{U}}} \cdot \underline{\underline{\boldsymbol{P}}}^{-1} \tag{3.10}$$

If the out of plane behaviour of the investigated material is of interest a 3D unit cell has to be used and the corresponding mean curvature tensor $\underline{\underline{\boldsymbol{\mathcal{X}}}}$ can be evaluated in a similar way as described in [19], cf. Eq. (3.11) where $\underline{\underline{\boldsymbol{R}}}$ indicates the rotation angles between top and bottom master nodes.

$$\underline{\underline{\boldsymbol{R}}} = \underline{\underline{\boldsymbol{\mathcal{X}}}} \cdot \underline{\underline{\boldsymbol{P}}} \qquad \underline{\underline{\boldsymbol{\mathcal{X}}}} = \underline{\underline{\boldsymbol{R}}} \cdot \underline{\underline{\boldsymbol{P}}}^{-1} \tag{3.11}$$

In order to apply macroscopic stress states $\underline{\underline{\boldsymbol{\Sigma}}}^M$ or the respective surface tractions $\underline{\boldsymbol{T}}^{M,k}$ using the master node concept, the following relation is obtained by employing the divergence theorem ([3])

$$F_i^k = \int\limits_{\Gamma_k} T_i^{M,k} \; d\Gamma \qquad T_i^{M,k} = \Sigma_{ji}^M \; n_j^k \tag{3.12}$$

where the index k indicates the master node, Γ_k and n_j^k the corresponding surface and normal vector, $T_i^{M,k}$ the traction vector related to the far field load along Γ_k and F_i^k the master node force. The opposite way, gaining the homogenized (macroscopic) stress tensor $\underline{\underline{\boldsymbol{\Sigma}}}$ from the master node forces is conducted as follows. Considering Eq. (3.12), the traction $T_i^{PK1,k}$ along the surface Γ_k slaved to the master node k is evaluated as

$$T_i^{PK1,k} = \frac{F_i^k}{A_0^k} \tag{3.13}$$

with A_0^k as the area of Γ_k at the undeformed state. The superscript $PK1$ indicates the connection to the first Piola Kirchhoff stress tensor which is discussed in the following section. Eq. (3.14) shows the relation between the traction $T_i^{PK1,k}$ and the corresponding stress tensor $\Sigma_{ji}^{PK1,k}$.

$$T_i^{PK1,k} = \Sigma_{ji}^{PK1,k}\ n_{0j}^k \tag{3.14}$$

n_{0j}^k describes the vector normal to the surface Γ_k at the undeformed state and is perpendicular to the respective periodicity vector p_i^k.

Now, that the application of loads and displacements and also the evaluation of homogenized (mean) stress and strain fields using the master node concept have been explained, the occurring stress and strain measures shall be discussed in more detail as already referred above.

3.1.3 Nonlinear Stress and Strain Measures

Although geometric nonlinearities may appear, the use of linearized stress and strain relations for homogenization and the application of far field loads would be sufficient in most cases. However, the formulations above give rise to nonlinear measures and in order to keep consistency a short summary of stress and strain measures and the corresponding transformations shall be given. A more detailed description can be found in [1] which also represents the basis for the remarks below.

The motion of a material body can be described by the motion of its material points where rigid-body displacements and deformations can occur. If those material points are mapped onto the Euclidian space each of them is assigned to a spatial point. Prescribing a fixed reference frame, the position of a material point can be described by the position vector $\underline{\boldsymbol{x}}(t)$ for every point in time t. Additionally a reference configuration $\underline{\boldsymbol{a}}$ at the reference time t_0 is introduced, cf. Eq. (3.15), which uniquely marks a specific material point.

$$\underline{\boldsymbol{x}}(t_0) = \underline{\boldsymbol{a}} \tag{3.15}$$

The motion of a specific material point can then be described as trajectory within a cartesian coordinate system according to Eq. (3.16) and is illustrated in Fig. 3.5.

$$x_i = x_i(a_j, t) \tag{3.16}$$

Here, a specific material point is chosen and the change of related quantities is described with respect to this point. This approach is known as Lagrangian description. Since the deformation of a body is described by Eq. (3.16), a deformation gradient tensor $\underline{\underline{\boldsymbol{F}}}$ can be introduced, which maps line elements from the reference configuration $d\underline{\boldsymbol{a}}$ to the current configuration $d\underline{\boldsymbol{x}}$ as illustrated in Fig. 3.6.

$$F_{ij} = \frac{\partial x_i}{\partial a_j} \qquad d\underline{\boldsymbol{x}} = \underline{\underline{\boldsymbol{F}}} \cdot d\underline{\boldsymbol{a}} \tag{3.17}$$

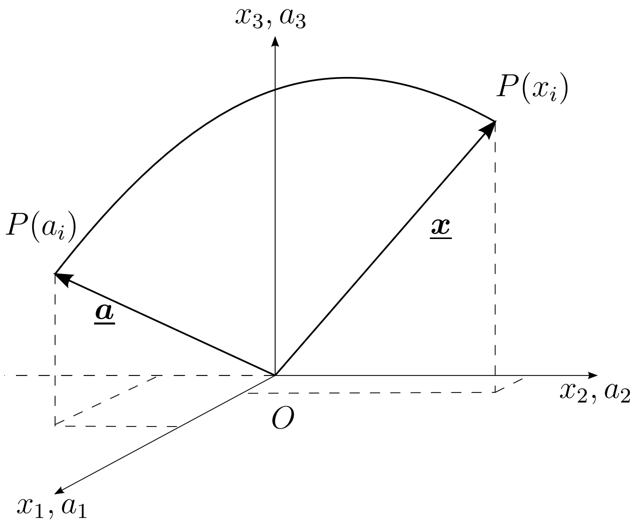

Figure 3.5: Trajectory of a material point P from the reference state $\underline{\boldsymbol{a}}$ to an arbitrary state $\underline{\boldsymbol{x}}$. [1]

The transformation of area elements follows accordingly. An area element of the reference configuration is defined by two corresponding line elements, Eq. (3.18) top, just as the one of the current configuration, Eq. (3.18) bottom.

$$\begin{aligned} d\underline{\boldsymbol{A}}_0 &= d\underline{\boldsymbol{a}}_1 \times d\underline{\boldsymbol{a}}_2 \\ d\underline{\boldsymbol{A}} &= d\underline{\boldsymbol{x}}_1 \times d\underline{\boldsymbol{x}}_2 = (\underline{\underline{\boldsymbol{F}}} \cdot d\underline{\boldsymbol{a}}_1) \times (\underline{\underline{\boldsymbol{F}}} \cdot d\underline{\boldsymbol{a}}_2) \end{aligned} \tag{3.18}$$

After some manipulations the following relation is obtained.

$$d\underline{\boldsymbol{A}} = (det\underline{\underline{\boldsymbol{F}}})(\underline{\underline{\boldsymbol{F}}}^T)^{-1} \cdot d\underline{\boldsymbol{A}}_0 \tag{3.19}$$

Finally the transformation of a volume element is defined in Eq. (3.20)

$$\begin{aligned} dV_0 &= |(d\underline{\boldsymbol{a}}_1 \times d\underline{\boldsymbol{a}}_2) \cdot d\underline{\boldsymbol{a}}_3| \\ dV &= |(d\underline{\boldsymbol{x}}_1 \times d\underline{\boldsymbol{x}}_2)| \cdot d\underline{\boldsymbol{x}}_3| \\ dV &= |det\underline{\underline{\boldsymbol{F}}}|dV_0 \end{aligned} \tag{3.20}$$

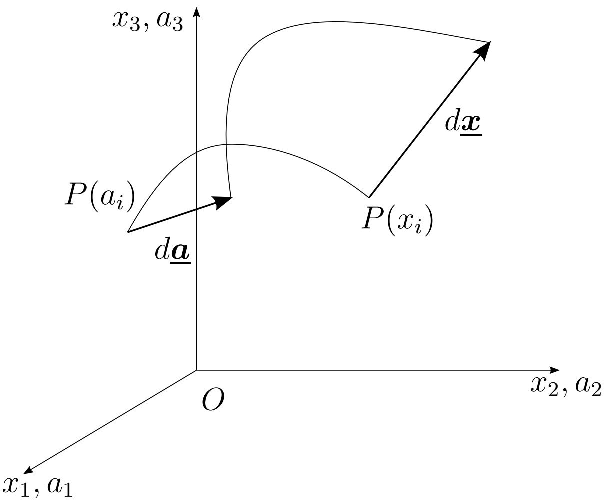

Figure 3.6: Transformation of a line element $d\underline{\boldsymbol{a}}$ of the reference configuration to the current configuration $d\underline{\boldsymbol{x}}$. [1]

The deformation of a body described in Eq. (3.16) can also be formulated in terms of displacements u_i.

$$x_i = a_i + u_i(a,t) \tag{3.21}$$

The definition of the deformation gradient tensor, Eq. (3.17), then gives

$$\begin{aligned} F_{ij} &= \frac{\partial x_i}{\partial a_j} = I_{ij} + \frac{\partial u_i}{\partial a_j} \\ J_{ij} &= \frac{\partial u_i}{\partial a_j} \end{aligned} \tag{3.22}$$

with the displacement gradient tensor J_{ij}. Since the deformation gradient tensor F_{ij} and also the displacement gradient tensor J_{ij} still contain possibly occurring rigid body motions and furthermore refer to the current configuration as well as to the reference configuration they are not appropriate for measuring strains. Therefore the rigid body motions are eliminated via a polar decomposition of F_{ij},

$$\underline{\underline{\boldsymbol{F}}} = \underline{\underline{\boldsymbol{R}}} \cdot \underline{\underline{\boldsymbol{U}}} = \underline{\underline{\boldsymbol{V}}} \cdot \underline{\underline{\boldsymbol{R}}} \tag{3.23}$$

where $\underline{\underline{\boldsymbol{R}}}\cdot\underline{\underline{\boldsymbol{U}}}$ is termed right polar decomposition and $\underline{\underline{\boldsymbol{V}}}\cdot\underline{\underline{\boldsymbol{R}}}$ left polar decomposition. $\underline{\underline{\boldsymbol{U}}}$ and $\underline{\underline{\boldsymbol{V}}}$ cause dilatation or compression of a line element along their principal directions whereas $\underline{\underline{\boldsymbol{R}}}$ is orthogonal and responsible for a rigid body rotation. Thus the following deformation tensors are obtained.

$$\begin{aligned} \underline{\underline{\boldsymbol{U}}} &= (\underline{\underline{\boldsymbol{F}}}^T \cdot \underline{\underline{\boldsymbol{F}}})^{1/2} \qquad & \underline{\underline{\boldsymbol{C}}} &= \underline{\underline{\boldsymbol{U}}}^2 = (\underline{\underline{\boldsymbol{F}}}^T \cdot \underline{\underline{\boldsymbol{F}}}) \\ \underline{\underline{\boldsymbol{V}}} &= (\underline{\underline{\boldsymbol{F}}} \cdot \underline{\underline{\boldsymbol{F}}}^T)^{1/2} \qquad & \underline{\underline{\boldsymbol{B}}} &= \underline{\underline{\boldsymbol{V}}}^2 = (\underline{\underline{\boldsymbol{F}}} \cdot \underline{\underline{\boldsymbol{F}}}^T) \end{aligned} \tag{3.24}$$

An interpretation of the right stretch tensor $\underline{\underline{\boldsymbol{U}}}$, the left stretch tensor $\underline{\underline{\boldsymbol{V}}}$ and the right and left Cauchy-Green tensors $\underline{\underline{\boldsymbol{C}}}$ and $\underline{\underline{\boldsymbol{V}}}$ is given in [1] (pages 94-95). The Green-Lagrange strain tensor $\underline{\underline{\boldsymbol{G}}}$ is then defined according to Eq. (3.25), $\underline{\underline{\boldsymbol{I}}}$ denotes the identity tensor.

$$\underline{\underline{\boldsymbol{G}}} = \frac{1}{2}[\underline{\underline{\boldsymbol{C}}} - \underline{\underline{\boldsymbol{I}}}] \tag{3.25}$$

$\underline{\underline{\boldsymbol{G}}}$, in contrast to $\underline{\underline{\boldsymbol{F}}}$, represents a symmetric tensor and gives $\underline{\underline{\boldsymbol{G}}} = \underline{\underline{\boldsymbol{0}}}$ in the case of rigid body motions. Another popular strain measure is the so-called logarithmic strain or true strain, respectively. Motivated from uniaxial tension experiments where the strain rate is evaluated as the ratio of length change to current length the logarithmic strain definition, Eq. (3.26), can be generalized to three dimensions as shown in Eq. (3.27) ([6]).

$$d\varepsilon_{ln} = \frac{dl}{l} \qquad \varepsilon_{ln} = ln(\frac{l}{l_0}) \tag{3.26}$$

Here, the natural logarithm of the left stretch tensor $\underline{\underline{\boldsymbol{V}}}$ is evaluated using the method of spectral decomposition. Therefore the logarithm is applied to the eigenvalues λ_i of $\underline{\underline{\boldsymbol{V}}}$ which are then multiplied with the tensor built form the dyades of the normalized eigenvectors of $\underline{\underline{\boldsymbol{V}}}$.

$$\underline{\underline{\boldsymbol{\varepsilon}}}_{ln} = ln(\underline{\underline{\boldsymbol{V}}}) = ln(\lambda_i)\ \underline{\boldsymbol{n}}_i \otimes \underline{\boldsymbol{n}}_i \tag{3.27}$$

Now that the most relevant strain tensors have been defined the corresponding stress measures shall be discussed. According to the Euler-Cauchy stress principle, external loads generate distributed forces within a body which can be described as tractions $T_i(x_i, n_i, t)$ depending on the considered area dA and the respective normal vector n_i, compare Fig. 3.7. Thus, the Cauchy traction vector is defined as a measure for the internal load acting at a specific point.

$$T_i^{Ca.}(x_i, n_i, t) = \frac{df_i}{dA}. \tag{3.28}$$

Since this formulation depends not only on the location but also on the orientation of the considered plane, the stress state at a certain point is defined by the entirety of traction vectors arising from an infinte number of plane orientations. A more favourable characterization of the stress state is represented by the stress tensor, which is independent of the plane orientation. Therefore the Cauchy stress tensor $\underline{\underline{\boldsymbol{\sigma}}}^{Ca.}$ follows as

$$T_i^{Ca.} = \sigma_{ji}^{Ca.}\ n_j \tag{3.29}$$

where the superscript indicates that Cauchy measures are described. It shall be noted that these measures just refer to the current configuration, meaning that

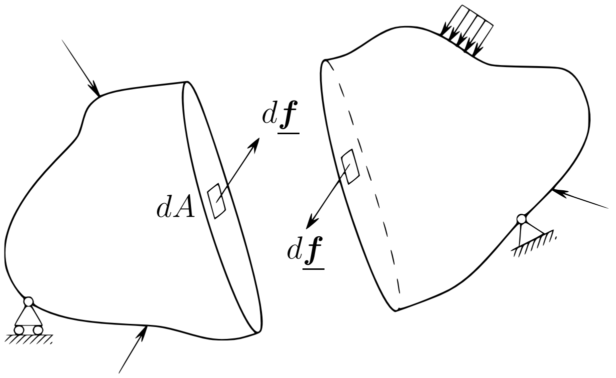

Figure 3.7: Illustration of the Euler-Cauchy stress principle. [1]

the current differential area element dA and normal vector n_i, cf. Eqs. (3.18) and (3.19), as well as the current differential force vector df_i are used to determine the stress state.

In some situations it is advantageous to refer to the reference configuration which is the case for the Piola-Kirchoff traction vectors and stress tensors. The first Piola-Kirchhoff traction vector refers the current differential force vector df_i to the differential area element of the reference configuration dA_0. The corresponding stress tensor is then defined according to Eq. (3.30), where n_{0j} denotes the normal vector of the considered plane in the reference configuration. Stresses defined in this way are also termed engineering stresses.

$$T_i^{PK1} = \frac{df_i}{dA_0} \qquad T_i^{PK1} = \sigma_{ji}^{PK1}\, n_{0j} \tag{3.30}$$

The second Piola-Kirchhoff traction vector and the corresponding stress tensor are completely defined in the reference configuration, as shown in Eq. (3.31), and have no straight physical meaning but the representation of the current stress state in the reference configuration.

$$T_i^{PK2} = \frac{df_{0i}}{dA_0} \qquad \underline{\underline{\boldsymbol{\sigma}}}^{PK2} = \underline{\underline{\boldsymbol{\sigma}}}^{PK1} \cdot \underline{\underline{\boldsymbol{F}}}^{-T} \tag{3.31}$$

df_{0i} denotes the differential force vector corresponding to the reference configuration. All the above mentioned stress measures can be transformed into each other by using the transformation rules for line and area elements, Eqs. (3.17) and (3.19).

$$\begin{aligned} \underline{\underline{\boldsymbol{\sigma}}}^{PK1} &= det(\underline{\underline{\boldsymbol{F}}})\underline{\underline{\boldsymbol{F}}}^{-1} \cdot \underline{\underline{\boldsymbol{\sigma}}}^{Ca.} \\ \underline{\underline{\boldsymbol{\sigma}}}^{PK2} &= det(\underline{\underline{\boldsymbol{F}}})[\underline{\underline{\boldsymbol{F}}}^{-1} \cdot \underline{\underline{\boldsymbol{\sigma}}}^{Ca.} \cdot \underline{\underline{\boldsymbol{F}}}^{-T}] \end{aligned} \tag{3.32}$$

When stress and strain tensors are linked together, special care has to be taken according their physical relation so that the specific internal power $\dot{e}$ gives identical values for conjugated tensors. The corresponding pairs for the presented tensors are given in Eq. (3.34), where the superscripted dot indicates the substantial derivative of the respective strain tensors.

$$\rho\dot{e} = \underline{\underline{\boldsymbol{\sigma}}}^{Ca.} \cdot\cdot\, \dot{\underline{\underline{\boldsymbol{\varepsilon}}}}_{ln}, \qquad \rho_0\dot{e} = \underline{\underline{\boldsymbol{\sigma}}}^{PK1} \cdot\cdot\, \dot{\underline{\underline{\boldsymbol{F}}}}, \qquad \rho_0\dot{e} = \underline{\underline{\boldsymbol{\sigma}}}^{PK2} \cdot\cdot\, \dot{\underline{\underline{\boldsymbol{G}}}} \tag{3.33}$$

ρ and ρ_0, respectively, denote the mass density and the double dot product ($\cdot\cdot$) is defined as

$$\underline{\underline{\boldsymbol{A}}} \cdot\cdot\, \underline{\underline{\boldsymbol{B}}} = A_{ij}\ B_{ji} \tag{3.34}$$

3.2 Material Nonlinearities

Besides the geometric description of the compound proper constitutive models have to be assigned to each of the constituents in order to obtain useful predictions of the overall material behaviour. The analyses carried out in this work utilize different material models and compare their effects on the predicted response. The following sections provide a short description of these models together with an approach for monitoring occurring nonlinearities.

3.2.1 Elasto-Brittle-Damage Model

This section describes a constitutive law capable of predicting the onset of damage and the post damage behaviour of transversally isotropic elastic-brittle materials. It is formulated in plane stress space and based on the assumptions that the undamaged material response is linear elastic and damage is initiated without plastic deformation. Hence, the influence of possibly occurring plasticity is neglected. However, fibre reinforced materials often exhibit such behaviour. This constitutive model has been proposed in [18] and is implement in the commercial finite element code Abaqus.

Damage initiation

In order to determine the onset of material degradation at a specific point the failure criterion proposed by Hashin [12] is used, which distinguishes between four different failure mechanisms: fibre tension ($\hat{\sigma}_{ll} \geq 0$),

$$F_{ft} = \left(\frac{\hat{\sigma}_{ll}}{X^T}\right)^2 + \alpha \left(\frac{\hat{\sigma}_{lq}}{S^L}\right)^2 = 1, \tag{3.35}$$

fibre compression ($\hat{\sigma}_{ll} < 0$),

$$F_{fc} = \left(\frac{\hat{\sigma}_{ll}}{X^C}\right)^2 = 1, \tag{3.36}$$

matrix tension ($\hat{\sigma}_{qq} \geq 0$),

$$F_{mt} = \left(\frac{\hat{\sigma}_{qq}}{Y^T}\right)^2 + \alpha \left(\frac{\hat{\sigma}_{lq}}{S^L}\right)^2 = 1, \tag{3.37}$$

and matrix compression ($\hat{\sigma}_{qq} < 0$),

$$F_{mc} = \left(\frac{\hat{\sigma}_{ll}}{2S^T}\right)^2 + \left[\left(\frac{Y^C}{2S^T}\right)^2 - 1\right] \frac{\hat{\sigma}_{qq}}{Y^C} + \left(\frac{\hat{\sigma}_{lq}}{S^L}\right)^2 = 1. \tag{3.38}$$

Although this criterion has shown to may not accurately predict the onset of failure it is widely used in industry. The criterion is based on a local coordinate system where l denotes the fibre direction and q the transverse in-plane direction. X^T and X^C are the tensile and compressive strengths in fibre direction, Y^T and Y^C

the tensile and compressive strengths in transverse in-plane direction and S^L and S^T the in-plane and transverse (out of plane) shear strengths.

Damage evolution

The stresses $\hat{\sigma}_{ij}$ denote effective stresses which are related to the nominal stresses according to Eq. (3.39) and the coefficient α controls the contribution of shear stress to the initiation criterion for fibre tension.

$$\begin{pmatrix} \hat{\sigma}_{ll} \\ \hat{\sigma}_{qq} \\ \hat{\sigma}_{lq} \end{pmatrix} = \begin{pmatrix} \frac{1}{1-d_f^{t,c}} & 0 & 0 \\ 0 & \frac{1}{1-d_m^{t,c}} & 0 \\ 0 & 0 & \frac{1}{1-d_s} \end{pmatrix} \begin{pmatrix} \sigma_{ll} \\ \sigma_{qq} \\ \sigma_{lq} \end{pmatrix} \tag{3.39}$$

The matrix acts as a damage operator with the damage variables $d_f^{t,c}$, $d_m^{t,c}$ and d_s for fibre, matrix and shear failure modes which range from 0 to 1. If no damage has occurred up to the current state $\hat{\sigma}_{ij} = \sigma_{ij}$. Once one of the criteria above is met, the effective stresses are used to determine the onset of other failure mechanisms and the propagation of the already activated ones. The damage variable corresponding to shear is assumed to be not independent in this model and the according relation is given below.

$$d_s = 1 - (1 - d_f^t)(1 - d_f^c)(1 - d_m^t)(1 - d_m^c) \tag{3.40}$$

Effect of Damage

Upon damage has occured the material response is computed from the relation

$$\underline{\boldsymbol{\sigma}} = \underline{\underline{\boldsymbol{C}}}^d \underline{\boldsymbol{\varepsilon}}, \tag{3.41}$$

where $\underline{\boldsymbol{\sigma}}$ and $\underline{\boldsymbol{\varepsilon}}$ are the vectors of stress/strain components according to Voigt notation and $\underline{\underline{\boldsymbol{C}}}^d$ denotes the damaged stiffness matrix, which is defined as follows.

$$\underline{\underline{\boldsymbol{C}}}^d = \frac{1}{D}\begin{pmatrix} (1-d_f^{t,c})E_l & (1-d_f^{t,c})(1-d_m^{t,c})\nu_{lq}E_l & 0 \\ (1-d_f^{t,c})(1-d_m^{t,c})\nu_{lq}E_q & (1-d_m^{t,c})E_q & 0 \\ 0 & 0 & (1-d_s)G_{lq}D \end{pmatrix}$$
$$D = 1-(1-d_f^{t,c})(1-d_m^{t,c})\nu_{lq}\nu_{ql} \tag{3.42}$$

E_l, E_q and G_{lq} are the undamaged material moduli and ν_{lq} and ν_{ql} the corresponding poisson ratios. The evolution of the damage variables is based on the fracture energy dissipated during the damage process and is controlled by equivalent displacements, which make sure that no mesh dependency is exhibited during strain softening. The relation between equivalent displacements and stresses shows a positive linear slope prior to damage initiation and a negative linear slope in the softening regime afterwards which is achieved by the evolution of the damage variables. The damage variable for each failure mode is then defined as

$$d_I = \frac{\delta_{I,eq}^{fail}(\delta_{I,eq}-\delta_{I,eq}^0)}{\delta_{I,eq}(\delta_{I,eq}^{fail}-\delta_{I,eq}^0)} \qquad I \in \{ft, fc, mt, mc\} \tag{3.43}$$

where $\delta_{I,eq}^0$ is the equivalent displacement at which the initiation criterion is met and $\delta_{I,eq}^{fail}$ the equivalent displacement for the fully damaged material. The equations for evaluating the equivalent displacements and stresses from the current stress and strain state are given in [18].

Since softening material behaviour and stiffness degradation can lead to convergence problems in implicit solution algorithms a viscous regularization scheme is implemented which ensures the tangent stiffness matrix of the softening material to be positive definite for sufficiently small time increments. Therefore viscous damage variables are introduced whereby the amount of energy dissipated due to viscous regularization shall be kept small in order to give reasonable material responses.

3.2.2 Elasto-Plasto-Damage Model

The constitutive model presented in the following has been developed by Flatscher [8] and aims at describing the nonlinear intra-ply behaviour of embedded plies in a composite laminate based on the plane stress assumption. Among various possible phenomena leading to a nonlinear material response, two basically different mechanisms are distinguished, namely stiffness degradation and accumulation of unrecoverable strains. The latter one is associated to inelastic microscopic matrix deformation and described by a multi-surface plasticity law whereas stiffness degradation is related to microscopic brittle matrix cracking, fibre matrix debonding and progressive fibre failure. These effects are modelled by brittle continuum damage mechanics where two approaches are considered, the first one addressing evenly distributed matrix dominated phenomena leading to strain hardening without damage localization and the second one accounting for localized matrix and fibre dominated phenomena leading to strain softening. All the above mentioned phenomena are combined in a single material law which reads, after integration of the loading history, as

$$\underline{\boldsymbol{\varepsilon}} = \underline{\boldsymbol{\varepsilon}}^{(el)} + \underline{\boldsymbol{\varepsilon}}^{(pl)} = \underline{\underline{\boldsymbol{C}}}\ \underline{\boldsymbol{\sigma}} + \underline{\boldsymbol{\varepsilon}}^{(pl)}. \tag{3.44}$$

$\underline{\boldsymbol{\varepsilon}}$ and $\underline{\boldsymbol{\sigma}}$ represent the vectors of strain and stress components, respectively, and $\underline{\underline{\boldsymbol{C}}}$ denotes the current compliance matrix. Hence, nonlinear effects are modelled through $\underline{\underline{\boldsymbol{C}}}$ and the vector of plastic strain components $\underline{\boldsymbol{\varepsilon}}^{(pl)}$.

Damage Initiation Criteria

The onset of damage is described by factors of material exertion for fibre and matrix material which are evaluated on the basis of Puck's failure surface,

$$F_P[\sigma_{ll}, \sigma_{qq}, \sigma_{lq}] = 0, \tag{3.45}$$

cf. [8]. The formulation is again based on a local ply coordinate system where l denotes the fibre direction and q the transverse in-plane direction. These factors are independent of the loading history and just reflect the current stress state. Therefore, the factor of matrix exertion $f_E^{(m)}$ is defined according to Eq. (3.46) where σ_{ij}° denotes the current stress state and $\sigma_{qq}^{\star}$ and $\sigma_{lq}^{\star}$ are determined so that $F_P[\sigma_{ll}^{\circ}, \sigma_{qq}^{\star}, \sigma_{lq}^{\star}] = 0$ holds.

$$\begin{pmatrix} \sigma_{qq}^{\circ} \\ \sigma_{lq}^{\circ} \end{pmatrix} = f_E^{(m)} \begin{pmatrix} \sigma_{qq}^{\star} \\ \sigma_{lq}^{\star} \end{pmatrix} \tag{3.46}$$

The factor of fibre exertion follows as

$$f_E^{(f)} = \max\left[\frac{\sigma_{ll}}{X^T}, \frac{-\sigma_{ll}}{X^C}\right] \tag{3.47}$$

where X^T and X^C denote the tensile and compressive strengths in fibre direction. Additionally, also the fracture plane orientation according to Puck's criteria is evaluated. Hence, a value of $f_E^{(m)} > 1$ depicts the onset of distributed brittle damage and upon a certain critical value of matrix exertion is reached also the localized brittle damage mechanism is activated whereas $f_E^{(f)} > 1$ immediately causes softening material behaviour.

Distributed brittle damage

This damage mechanism accounts for the stiffness degrading effect of evenly distributed, matrix dominated phenomena like microscopic matrix cracking and fibre matrix debonding. Therefore strain hardening is modelled since no damage localization is expected. The effect of these phenomena is represented by embedding fictitious spheroidal inhomogeneities into the undamaged, smeared out ply material, cf. [31]. These penny-shaped inhomogeneities with small aspect ratio are aligned according to the predicted fracture plane orientation and are either modelled as voids under transverse tensile loads or isotropic material properties are assigned in the case of transverse compressive loads. The volume fraction $\xi^{(m)}$ of the inhomogeneities directly represents the damage value and is computed according to Eq. (3.48), $k_d^{(m)}$ denotes the evolution parameter and has to be calibrated from experimental data.

$$\xi^{(m)} = k_d^{(m)} \left(f_E^{(m)} - 1 \right)^2 , \qquad f_E^{(m)} > 1 \tag{3.48}$$

Furthermore, always the maximum volume fraction $\xi^{(m)}$ occurred in the loading history is used for the stiffness computation in order to prevent decreasing damage values. Finally, the full compliance tensor $\underline{\underline{\boldsymbol{C}}}$ of the damaged material is evaluated utilizing a Mori-Tanaka like method, cf. [3].

$$\underline{\underline{\boldsymbol{C}}} = \left(\underline{\underline{\boldsymbol{I}}} + \sum_p \underline{\underline{\boldsymbol{D}}}^{(p)} \right) \underline{\underline{\boldsymbol{C}}}^{(0)} \tag{3.49}$$

$\underline{\underline{\boldsymbol{C}}}^{(0)}$ represents the undamaged compliance tensor, $\underline{\underline{\boldsymbol{I}}}$ the identity tensor and $\underline{\underline{\boldsymbol{D}}}^{(p)}$ represents the effect of the populations of inhomogeneities. A more detailed explanation is given in [8].

Localized brittle damage

The effect of localized failure is modelled as local stiffness degradation causing strain softening behaviour where the same micromechanical approach as for distributed brittle damage is utilized. Thus, additional fictitious inhomogeneities with the same shape as for distributed damage are introduced and aligned in fibre direction in order to capture progressive fibre failure. The characterization of damage evolution is conducted by introducing equivalent stresses and strains in a similar way as already outlined in the description of the elasto-brittle damage model above, cf. also [18], with the difference that exponential softening is assumed. Four failure modes are distinguished, fibre tension, fibre compression, matrix transverse tension and matrix transverse compression, where the equivalent stresses and strains at the onset of softening are related to the energy dissipation due to failure of the corresponding mode. The effect of localized brittle damage on the compliance matrix $\underline{\underline{\boldsymbol{C}}}$ is evaluated similar to Eq. (3.49).

$$\underline{\underline{\boldsymbol{C}}} = \underline{\underline{\boldsymbol{C}}}^{(0)} + \underline{\underline{\boldsymbol{D}}}\,\underline{\underline{\boldsymbol{C}}}^{(0)} = \underline{\underline{\boldsymbol{C}}}^{(0)} + \frac{\xi}{1-\xi}\,\underline{\underline{\boldsymbol{N}}}^{(0)} \tag{3.50}$$

$\underline{\underline{\boldsymbol{N}}}^{(0)}$ is an auxiliary matrix and ξ denotes a generalized amount of damage as the volume fractions of inhomogeneities originating from the active failure modes where the evolution of these volume fractions is driven by a scalar damage evolution parameter. The evolution parameter itself strongly depends on the exponential softening law which is thus determining the propagation of damage. It shall be noted that this damage mechanism, once a certain matrix exertion factor $f_E^{(m)}$ is reached, also influences the evolution of volume fractions of those inhomogeneities originating from the distributed damage mechanism.

Multi-surface plasticity

Loading and unloading loops during experimental testing have shown that, besides the already described elasto-brittle behaviour, the occurrence of unrecoverable strain accumulation may be observed. This phenomenon is captured by an incorporated multi-surface plasticity model which assumes the plastic shear strains to be driven by tractions along planes parallel to the fracture planes predicted according to Puck's criteria (shear planes). The evolution of plastic strains is then modelled by two plasticity mechanisms where each of them is assigned to specific shear planes and controlled by a characteristic shear stress component. Accordingly, these mechanisms, in-plane shear and transverse compression, represent the evolution of the respective characteristic plastic strain component. The first mechanism captures the ply behaviour under dominant shear loads thus accumulating the plastic shear strains $\gamma_{lq}^{(pl)}$ driven by the shear stress component σ_{lq} whereas the latter concerns the behaviour under dominant transverse compressive loads. Therefore, the plastic shear strains $\gamma_{nt}^{(pl)}$ accumulate controlled by the shear stress component σ_{nt}, where n denotes the direction normal to the inclined shear plane and t the transverse direction, accordingly. The yield criteria for the mechanisms follow as

$$\begin{aligned} f_I &= \sigma_I - \tilde{\sigma}_I = 0 \\ f_{II} &= \sigma_{II} - \tilde{\sigma}_{II} = 0 \end{aligned} \tag{3.51}$$

where $\sigma_{I,II}$ represents an equivalent stress which is determined in dependence of the current ratio of in-plane shear stress to transverse stress. The yield stress $\tilde{\sigma}_{I,II}$ is represented by a Ludwick type power law and the hardening behaviour is assumed to be linear in the amount of plastic flow. The contributions of both mechanisms are combined in order to give the total plastic strain rate.

$$\underline{\dot{\boldsymbol{\varepsilon}}}^{(pl)} = \underline{\dot{\boldsymbol{\varepsilon}}}_{I}^{(pl)} + \underline{\dot{\boldsymbol{\varepsilon}}}_{II}^{(pl)} \tag{3.52}$$

3.2.3 Drucker-Prager Plasticity

This section gives a short overview of the linear Drucker-Prager plasticity model in the form of its implementation in the commercial finite element code Abaqus, cf. [5]. In the context of this work it is meant to model the accumulation of unrecoverable strains in the unreinforced matrix pockets of a textile ply.

A plasticity model is defined by a yield condition, a flow rule and, if hardening shall be modelled, a hardening law. Before these attributes are given for the linear Drucker-Prager model, some basic definitions are introduced. Thus, the equivalent pressure stress p is defined as the negative hydrostatic part of the stress tensor, cf. Eq. (3.53).

$$p = -\frac{1}{3}\sigma_{ii} \tag{3.53}$$

Accordingly, the stress deviator tensor $\underline{\underline{\boldsymbol{S}}}$ follows as

$$\underline{\underline{\boldsymbol{S}}} = \underline{\underline{\boldsymbol{\sigma}}} + p\underline{\underline{\boldsymbol{I}}} \tag{3.54}$$

with the identity tensor $\underline{\underline{\boldsymbol{I}}}$. The Mises equivalent stress q then reads as

$$q = \sqrt{\frac{3}{2}\left(\underline{\underline{\boldsymbol{S}}} : \underline{\underline{\boldsymbol{S}}}\right)}. \tag{3.55}$$

The yield condition F for the linear Drucker-Prager plasticity model is defined according to Eq. (3.56),

$$\begin{aligned} F &= t - p\ \tan\beta - d = 0 \\ t &= \frac{1}{2}q\left[1 + \frac{1}{K} - \left(1 - \frac{1}{K}\right)\left(\frac{r}{q}\right)^3\right] \qquad r = \left(\frac{9}{2}\underline{\underline{\boldsymbol{S}}} \cdot \underline{\underline{\boldsymbol{S}}} : \underline{\underline{\boldsymbol{S}}}\right)^{\frac{1}{3}} \\ d &= \left(\frac{1}{K} + \frac{1}{3}\tan\beta\right)\sigma_t \end{aligned} \tag{3.56}$$

where β denotes the friction angle of the material and t defines the shape of the yield surface according to a cut in the deviatoric plane. K is the ratio of the yield stress in triaxial tension to the one in triaxial compression. A value of $K = 1$ results in a circular, Mises-like shape of a cross-section in the deviatoric plane. r represents the third invariant of the deviator stress tensor and d denotes the cohesion of the material with the uniaxial tensile yield stress σ_t. In the case of $K = 1$ the resulting yield surface represents a cone in principal stress space where its axis of rotation is aligned to the hydrostatic axis and the peak is pointing towards increasing values. The flow rule is defined through the flow potential G, cf. Eq. (3.57), with the dilation angle ψ.

$$G = t - p\ \tan\psi \tag{3.57}$$

If $\psi = \beta$ associated flow is modelled. Considering the Abaqus implementation, hardening behaviour can be specified by directly entering yield stress values versus equivalent plastic strain. The other input variables are the friction angle β, the dilation angle ψ and the yield stress ratio K.

3.2.4 Assessing Nonlinearities

This chapter so far described a micromechanical modelling approach for investigating composite laminates together with some advanced constitutive models to be applied. The corresponding unit cell simulations completely describe the nonlinear material response with all phenomena incorporated in the respective constitutive model. However, the question arises of how the current loading state can be assessed with respect to a quantity which identifies e.g. specific damage/plasticity states and thus provides a measure for comparing different loading situations with respect to induced damage/plasticity. Although the occurring phenomena could be described via the corresponding stress and strain tensors, a more straightforward way is represented by the respective dissipated energies, which are, additionally, directly accessible from FEM simulations. Considering an example of an uniaxial stress-strain relation, the contributions of different mechanisms to the total strain energy density can be easily visualized, cf. Fig. 3.8 where w_{dam} denotes the dissipated energy density due to damage, w_{pla} the dissipated energy density due to plasticity and w_{rec} the recoverable strain energy density. Hence, if plasticity and

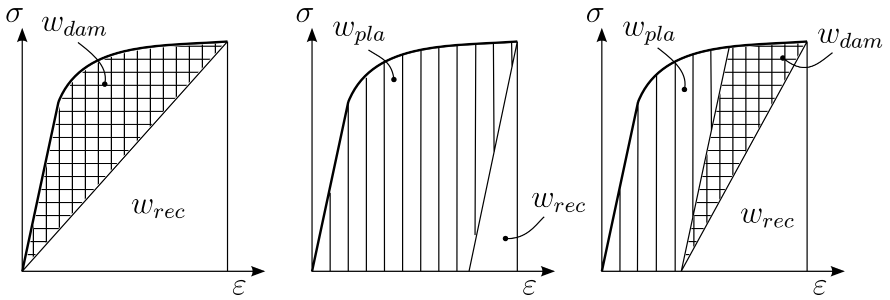

Figure 3.8: Visualization of the contributions of different phenomena to the total strain energy in the case of uniaxial stress-strain curves. The situation when just damage occurs is depicted on the left side, just plasticity in the middle and both phenomena combined on the right side, cf. [10]. For the combined situation it is assumed that, at the beginning, just plasticity occurs while from the onset of damage the plastic strains stay constant.

damage are the considered nonlinear mechanisms the total strain energy density is given by Eq. (3.58).

$$w_{tot} = w_{rec} + w_{dam} + w_{pla} \tag{3.58}$$

These energy dissipations allow for a distinct assignment of the occurring nonlinearity to the causing mechanism and thus represent suitable quantities for assessing the current loading state. Furthermore it has been shown, in the case of damage, cf. [7], that nonlinear material behaviour due to progressing damage can be described by choosing the dissipated energy as the damage parameter in the constitutive model which confirms the choice of these quantities as measure for nonlinearities. In order to generalize this approach, the respective dissipated energy densities are normalized using the current total strain energy density w_{tot}. The resulting energy fractions p_i, cf. Eq. (3.59), are then used to determine the material utilization as described in the following chapter.

$$p_i(t) = \frac{w_i(t)}{w_{tot}(t)}, \qquad i \in \{dam, pla, ...\} \tag{3.59}$$

The parameter t in Eq. (3.59) denotes the current load magnitude during a simulation (simulation time). This characterization is not just restricted to damage and plasticity but can also be extended to describe delamination, friction and other mechanisms.

Chapter 4

Energy Dissipation Monitoring

The prediction of the nonlinear behaviour of textile composites by numerically solved unit cell models is computationally demanding and therefore limited to small domains. In order to extend the predictional capabilities to large structures a two step procedure is proposed which combines linear elastic structural analyses with nonlinear unit cell simulations. To this end, in a first step, occurring nonlinear mechanisms are systematically investigated by conducting unit cell simulations for a distribution of plane stress states comprising appropriate constitutive laws, as described in Chapter 3, while monitoring the dissipated energies corresponding to the respective mechanisms. Those are easily accessible from FEM simulations and the resulting energy fractions, cf. Eq. (3.59), are used to assess the loading state and generate envelopes for individual mechanisms. This procedure is described in the first part of this chapter. In a second step, a methodology for mapping the information gained from unit cell simulations to large scale linear elastic analyses as a post-processing option is proposed and presented in the second part of this chapter. Parts of this concept have already been presented at the 19th International Conference on Composite Materials [10].

4.1 Generating Envelopes

Considering a general example of a nonlinear unit cell simulation, the basic quantities describing the nonlinear response are represented by the homogenized stress and strain states and the corresponding dissipated energies at each load increment of the simulation. A generic example of how these quantities are related to each other is given in Fig. 4.1 for the case of uniaxial loading. Depending on the applied constitutive model, at some load increment nonlinear mechanisms are initiated and start to develop according to the implemented evolution law. This onset of dissipative mechanisms causes stiffness degradation and inelastic strains resulting in a nonlinear stress-strain relation. The values of the dissipated energy fractions are assigned to the stress-strain state according to the current load level t^*, as illustrated in Fig. 4.1, which allows for an assessment of the load state for each simulated increment $t_0 \leq t^* \leq t_{end}$. However, this assessment corresponds to one specific load case with a defined relation between each load increment, which will be referred to as load path. In order to be able to assess arbitrary stress and strain

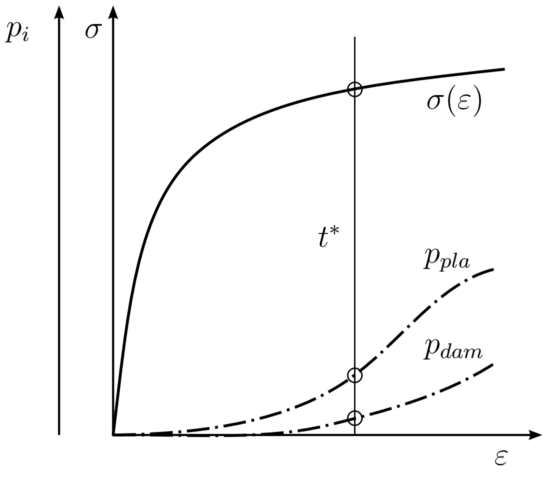

Figure 4.1: Sketch of a uniaxial stress-strain relation with the corresponding dissipated energy fractions p_i. t^* denotes the load level under consideration.

states, respectively, regarding their corresponding dissipated energy fractions p_i, simulations of an infinite number of load paths are necessary.

This demand can be reduced to just cover plane stress states without significant loss in applicability since textile composites are mostly used in thin walled structures. Furthermore, a discretization of plane stress space reduces the number of states necessary to be simulated where intermediate states are interpolated accordingly, cf. Fig. 4.2 left. However, since nonlinear dissipative behaviour is load history dependent, meaning that the stress-strain state and the corresponding energy fractions p_i at a specific load increment t^* depend on the currently applied load but also on every load state applied before ($t \leq t^*$), it is not sufficient to compute just one load path for each selected state (point) in plane stress space. Thus, all possible curves (load paths) connecting the origin (unloaded state) with the selected point (state) in plane stress space have to be computed in order to entirely describe and assess the selected state, cf. Fig. 4.2 right. This obviously

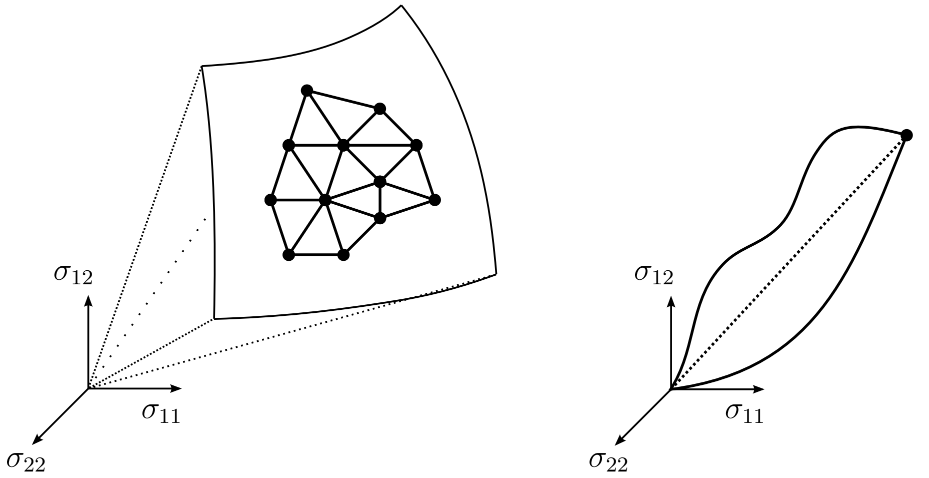

Figure 4.2: Possible discretization illustrated for a selected range of plane stress states (left) and depiction of three different load paths leading to the same state in plane stress space, but, different strain states (right). The straight dotted line represents proportionally increasing stress components and, thus, depicts a radial stress path.

continuous system shall now be reduced to a discrete one by assuming that the set of all load paths leading to one specific state can be approximated by several straight (radial) paths which enclose the specific path under consideration. This assumption, together with the simplifications mentioned above, finally allows to assess arbitrary stress and strain states by simulating a finite number of specifically chosen radial load paths. A method for choosing radial load paths related to one specific plane stress state so that they enclose all other paths related to this state is proposed in the following section.

4.1.1 Radial Load Paths

In general, a radial load path is represented by the proportional increase of all stress tensor components, cf. Fig. 4.2 right where an example of a radial stress path in plane stress space is illustrated as a dotted line. Since not only stresses can be applied as loads but also strains, the existence of radial strain paths follows consequently.

Considering the material behaviour in the linear elastic regime, stress and strain states are independent of the loading history meaning that the simulation of just one radial stress path related to a selected plane stress state is enough to predict all quantities corresponding to this state. Furthermore, every plane stress state represented by a point in plane stress space can be uniquely related to a corresponding strain state according to the linear elastic stiffness of the textile composite under consideration thus giving rise to an associated radial strain path. As long as the linear elastic regime is not left, the simulation of this radial strain path is equivalent to the simulation of the related radial stress path. However, once dissipative mechanisms are activated the uniqueness of the relation between the discussed stress and strain states is lost due the load history dependence and the results obtained through radial stress or strain paths differ. In order to avoid the simulation of an infinite number of combinations of paths leading to the same state as discussed above, an analogy from micromechanics shall be applied in a heuristic manner. There, upper and lower bounds for the elastic properties of inhomogeneous materials depending on the volume fraction of the inhomogeneities are stated in following way. Assuming perfect bonding between the constituents, a lower bound, known as Reuss bound [29], for the elastic properties is found by assuming uniaxial transverse loading, cf. Fig. 4.3 left. In this situation, the stress states in fibres and matrix are equal to the applied stress $\sigma_\infty = \sigma_f = \sigma_m$ leading to a constant stress state in the composite. In order to evaluate a lower bound for the elastic modulus the rule of mixtures is then applied on the compliance components. The right situation in Fig. 4.3 leads to a constant strain state in the composite for perfectly bonded constituents, $\varepsilon_\infty = \varepsilon_f = \varepsilon_m$, and gives an upper bound for the elastic properties, known as Voigt bound [34]. Thus, applying the rule of mixtures on the stiffness components yields the upper bound for the elastic modulus. The combination of both bounds in tensorial form is known as Hill

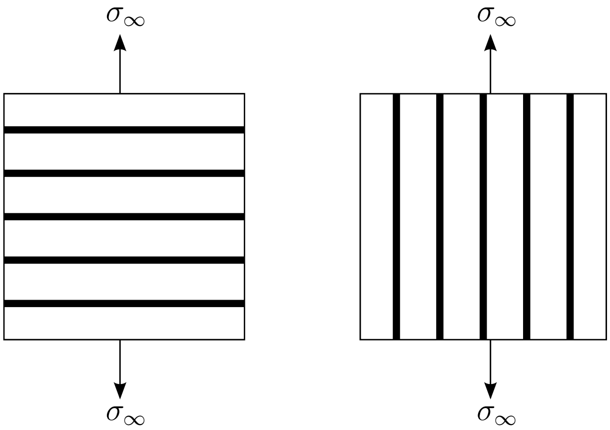

Figure 4.3: Uniaxial loading of a continuous fibre reinforced composite. The left situation corresponds to the situation for evaluating lower bounds of the elastic properties according to Reuss [29] and the right one gives the corresponding upper bounds according to Voigt [34].

bounds [13]. In the present case, estimates for the dissipated energy fractions p_i at certain (plane) stress states shall be stated in a similar way as the Hill bounds for the elastic properties. Therefore, some lower estimate may be assumed to be given by simulating a radial stress path containing the desired (plane) stress state. Accordingly, the upper bound is supposed to be related to a radial strain path where the corresponding strain state is approximated by using the linear elastic stiffness of the composite. These stress and strain states are uniquely related in the linear elastic regime but once nonlinear mechanisms occur this property is lost and the corresponding radial stress and strain paths are assumed to represent lower and upper estimates for the dissipated energy fractions. Therefore, the computation of these two paths for each given (plane) stress state is sufficient for entirely describing this state.

Radial Stress Paths

In a first step, radial stress paths are considered. Since arbitrary (plane) stress states shall be covered several paths have to be investigated so that whole plane stress space is covered. In the case of some microgeometries of textile composites, symmetries may be utilized in order to reduce the domain to be investigated, but, for the sake of generality these properties are not discussed in the following.

Now, a suitable discretization of plane stress space is needed. Obviously, the more paths are taken into consideration the more precise the prediction for different states will be. However, a beneficial spatial variation of the paths in terms of resolution and computational effort is not known a priori and thus has to be determined iteratively for each textile composite under consideration. A first try may be represented by evenly distributed paths modelling a sphere in plane stress space as proposed in [20]. Therefore, a specific stress path i is represented by the vector of stress components $\underline{\boldsymbol{\sigma}}^i$ which can be splitted into a directional unit vector $\underline{\boldsymbol{d}}^i$ and a scalar multiplier s_{max} determining the length of $\underline{\boldsymbol{\sigma}}^i$.

$$\underline{\boldsymbol{\sigma}}^i = \begin{pmatrix} \sigma_{11}^i \\ \sigma_{22}^i \\ \sigma_{12}^i \end{pmatrix} \qquad \underline{\boldsymbol{\sigma}}^i = s_{max}\ \underline{\boldsymbol{d}}^i \tag{4.1}$$

$\underline{\boldsymbol{d}}^i$ is then given according to a suitable distribution of points in plane stress space and s_{max} is chosen to be high enough so that the investigated nonlinear mechanisms are clearly recognizable. The resulting stress states represent the homogenized (far field) stresses in terms of the unit cell analysis and the equivalent boundary conditions are determined according to Eq. (3.12).

Besides the spatial resolution of the predictions also the radial discretization shall be discussed. Since the onset and evolution of the dissipated energy fractions shall be tracked along each path it is essential to provide a small load (time) increment for the simulation so that enough points along the path are computed. After all paths of interest have been simulated, each of them can be scanned for stress and strain states where certain energy fractions p_i are met. The gathered points can then be marked in plane stress space and form an envelope for a defined value of the energy fraction of a chosen mechanism. Thus, the occurrence and the directional sensitivity of each mechanism can be visualized. Furthermore, the gained information can be stored in a database in order to allow for an automated assessment of specified stress states. This procedure will be discussed in section 4.2.

Simulations of radial stress paths for investigating nonlinear material behaviour of textile composites have already been done by Meindlhumer [20], whose work is directly continued in this thesis.

Radial Strain Paths

The definition of radial strain paths follows directly from the radial stress paths discussed above by transforming the corresponding plane stress state via the linear elastic stiffness of the textile composite under consideration. The obtained strain state is then used to define a straight (radial) path in plane strain space. Although different strain states could be related to the specified stress state, the choice of the linear elastic relation follows from the motivation that the obtained information shall be applied on the results of linear elastic simulations of large structures.

First, the stiffness of the textile composite has to be evaluated. Since the modelling strategy described in Chapter 3 implies that the behaviour of thin layers is considered, the constitutive relation for shells is used, cf. Eq. (4.2).

$$\begin{pmatrix} \underline{\boldsymbol{N}} \\ \underline{\boldsymbol{M}} \end{pmatrix} = \begin{pmatrix} \underline{\underline{\boldsymbol{A}}} & \underline{\underline{\boldsymbol{B}}} \\ \underline{\underline{\boldsymbol{B}}} & \underline{\underline{\boldsymbol{D}}} \end{pmatrix} \begin{pmatrix} \underline{\bar{\boldsymbol{\varepsilon}}} \\ -\underline{\boldsymbol{\chi}} \end{pmatrix} \tag{4.2}$$

$\underline{\boldsymbol{N}}$ and $\underline{\boldsymbol{M}}$ are the stress resultants (membrane forces and bending moments) according to Eq. (4.3), i.e. the components of the stress tensor integrated over the thickness h of the considered cross-section, $\underline{\bar{\boldsymbol{\varepsilon}}}$ represents the membrane strains and $\underline{\boldsymbol{\chi}}$ the curvature changes, both in Voigt notation.

$$\begin{aligned} \underline{\boldsymbol{N}} &= \begin{pmatrix} N_{11} \\ N_{22} \\ N_{12} \end{pmatrix} & \qquad \underline{\boldsymbol{M}} &= \begin{pmatrix} M_{11} \\ M_{22} \\ M_{12} \end{pmatrix} \\ N_{ij} &= \int_{-h/2}^{h/2} \sigma_{ij}\ dx_3 & \qquad M_{ij} &= \int_{-h/2}^{h/2} \sigma_{ij} x_3\ dx_3 \end{aligned} \tag{4.3}$$

The matrix containing the submatrices $\underline{\underline{\boldsymbol{A}}}$, $\underline{\underline{\boldsymbol{B}}}$ and $\underline{\underline{\boldsymbol{D}}}$ depicts the (6x6) shell stiffness matrix where $\underline{\underline{\boldsymbol{A}}}$, $\underline{\underline{\boldsymbol{B}}}$ and $\underline{\underline{\boldsymbol{D}}}$ are called extensional, coupling and bending stiffness matrices. In order to determine the 36 components of the ABD matrix, 6 linearly independent load cases need to be evaluated. These can be, for example, tension in 1-direction, tension in 2-direction, shear, bending around the 1-axis, bending around the 2-axis and twist. Now equation systems for each line of the ABD matrix can be set up and solved consecutively thus determining all components.

Consequently, the already selected radial stress paths $\underline{\boldsymbol{\sigma}}^i$ are transformed according to Eq. (4.2) after the corresponding stress resultants have been evaluated. Within the scope of this work, the curvature changes are set to be $\underline{\boldsymbol{\chi}} = \underline{\boldsymbol{0}}$ and just the extensional stiffness matrix $\underline{\underline{\boldsymbol{A}}}$ and the membrane stress and strain states, $\underline{\boldsymbol{N}}$ and $\underline{\bar{\boldsymbol{\varepsilon}}}$, are considered. Therefore the radial strain paths i are expressed as follows.

$$\underline{\bar{\boldsymbol{\varepsilon}}}^i = e_{max}\, \underline{\boldsymbol{d}}^i_{\varepsilon} \tag{4.4}$$

e_{max} defines the length of the strain paths and is chosen in the same way as s_{max} and $\underline{\boldsymbol{d}}^i_{\varepsilon}$ represents the directional unit vector in plane strain space. The boundary conditions for the subsequent unit cell analyses are evaluated according to Eq. (3.9), where $\underline{\bar{\boldsymbol{\varepsilon}}}^i$ corresponds to the homogenized (far field) strains. For the avoidance of doubt it shall be clarified that the considered states, visualized as radial paths in plane strain space, are still plane stress states since the out of plane deformation is not prescribed to be zero. The corresponding boundaries are modelled traction free in both cases. As already described for radial stress paths, the results can be used for generating surfaces (envelopes) of constant energy fractions p_i in plane stress space and, furthermore, a database for automated post-processing can be set up.

4.2 Assessing nonlinearities in large structural components

After the computation of all considered radial stress and strain paths through nonlinear unit cell analyses the question arises of how these results can be combined with linear elastic simulations of large structural components. First every stress/ strain state obtained in the linear elastic structural analysis has to be mapped appropriately to the corresponding nonlinear state so that the associated energy fractions p_i can be related to the linear elastic states. Since a finite number of paths is computed the energy fractions are interpolated for intermediate states and their evolution is evaluated in terms of proportional load increase.

In order to allow for an automated post processing of arbitrary linear elastic stress analyses, the results of all simulated paths are stored in a database and the described methodology is completely scripted and implemented in the commercial finite element code Abaqus. Thus, once a database for a specific material system has been generated, the assessment of arbitrary linear elastic stress states can be done within seconds independently from the complexity of the investigated component.

4.2.1 Linking Mesoscale and Macroscale

The starting point of the proposed post-processing methodology is represented by the linear elastic stress state $\underline{\boldsymbol{\sigma}}_{lin}$ of interest and the corresponding strain state $\underline{\boldsymbol{\varepsilon}}_{lin}$, both represented in Voigt notation. However, the entire state $(\underline{\boldsymbol{\sigma}}_{lin}, \underline{\boldsymbol{\varepsilon}}_{lin})$ may be inaccessible in terms of the conducted unit cell analyses since nonlinear mechanisms can already be active at the investigated state. Hence, either equal stress states or equal strain states can be compared, cf. Eq. (4.5). Furthermore, both combinations in Eq. (4.5) can be applied on radial stress and radial strain paths for determining the energy fractions p_i related to the state $(\underline{\boldsymbol{\sigma}}_{lin}, \underline{\boldsymbol{\varepsilon}}_{lin})$. In order to reduce the number of possible combinations and to keep a consistent formulation, equal stress states (Eq. (4.5) top) are considered along radial stress paths and equal strain states (Eq. (4.5) bottom) are considered along radial strain paths.

$$\begin{aligned} \underline{\boldsymbol{\sigma}}_{nl}(\underline{\boldsymbol{\varepsilon}}_{nl}) &= \underline{\boldsymbol{\sigma}}_{lin}(\underline{\boldsymbol{\varepsilon}}_{lin}), \qquad \underline{\boldsymbol{\varepsilon}}_{nl} \neq \underline{\boldsymbol{\varepsilon}}_{lin} \\ \underline{\boldsymbol{\varepsilon}}_{nl}(\underline{\boldsymbol{\sigma}}_{nl}) &= \underline{\boldsymbol{\varepsilon}}_{lin}(\underline{\boldsymbol{\sigma}}_{lin}), \qquad \underline{\boldsymbol{\sigma}}_{nl} \neq \underline{\boldsymbol{\sigma}}_{lin} \end{aligned} \tag{4.5}$$

This procedure is illustrated in Fig. 4.4, where the energy fractions corresponding to a specified linear elastic state are evaluated for equal stress states (left) and equal strain states (right). The left situation corresponds to the unit cell response of the related radial stress path whereas the right situation depicts the response of the related radial strain path. The determined energy fractions are denoted

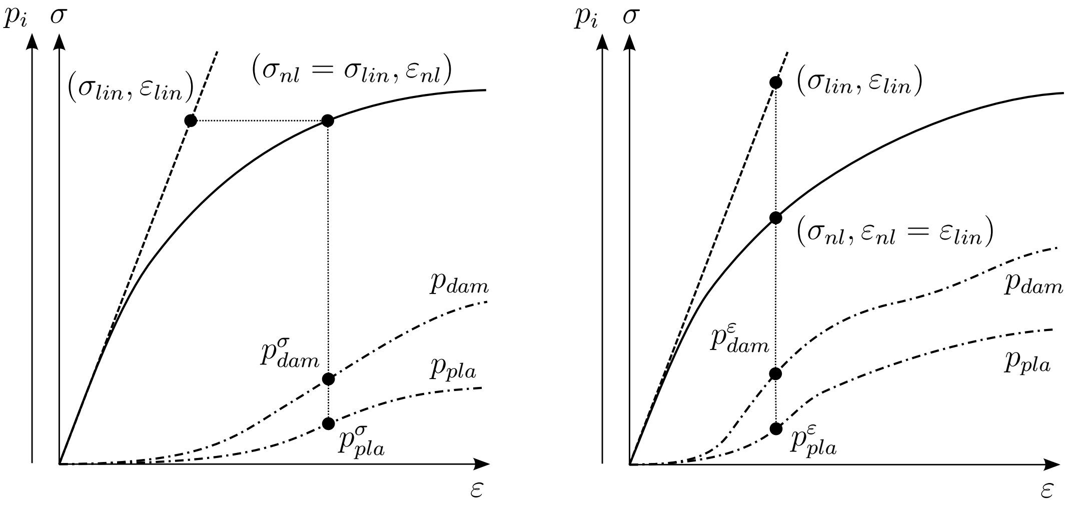

Figure 4.4: Example of the relation between the linear elastic state obatined from a structural analysis and the nonlinear unit cell response for radial stress paths (left) and radial strain paths (right) in the case of uniaxial loading.

as p_i^σ and p_i^ε, where the superscript indicates whether stress or strain states are compared. At this point it shall be mentioned that the described procedure for mapping linear to nonlinear states has a recognizable influence on the determined values for p_i^σ and p_i^ε and may lead to $p_i^\sigma > p_i^\varepsilon$. Although this circumstance may seems contradicting to the assumption that radial stress and strain paths represent lower and upper bounds for the dissipated energy fractions, the situation is just occurring due to the mapping itself.

In order to circumvent this methodological influence another additional procedure for mapping linear to nonlinear states is proposed. Considering the linear elastic state $(\underline{\boldsymbol{\sigma}}_{lin}, \underline{\boldsymbol{\varepsilon}}_{lin})$ at a certain material point, this state can also be expressed by means of the corresponding total strain energy density w_{tot}, cf. Eq. (4.6), where the general relation through integration and also the simplified one for the linear case are stated. All vectors in Eq. (4.6) are written in Voigt notation and represent the vectors of stress and strain components.

$$w_{tot} = \int \underline{\boldsymbol{\sigma}}^T \, d\underline{\boldsymbol{\varepsilon}} \qquad w_{tot}^{lin} = \frac{1}{2} \, \underline{\boldsymbol{\sigma}}_{lin}^T \, \underline{\boldsymbol{\varepsilon}}_{lin} \tag{4.6}$$

Now, two related states are represented by equal strain energy densities $w_{tot}^{nl} = w_{tot}^{lin}$, where w_{tot}^{nl} is the total strain energy density corresponding to the nonlinear unit cell simulations, cf. Eq. (3.58). This condition can also be formulated as follows.

$$\int_0^{\underline{\boldsymbol{\varepsilon}}_{nl}} \underline{\boldsymbol{\sigma}}_{nl}^T \, d\underline{\boldsymbol{\varepsilon}} = \frac{1}{2} \, \underline{\boldsymbol{\sigma}}_{lin}^T \, \underline{\boldsymbol{\varepsilon}}_{lin} \tag{4.7}$$

In the case of uniaxial loading Eq. (4.7) requires that the areas below the corresponding stress-strain curves are equal, cf. Fig. 4.5. This procedure is applied on both, radial stress and strain paths, and the determined dissipated energy fractions are denoted as $p_i^{w(\sigma)}$ and $p_i^{w(\varepsilon)}$, where the superscripts $w(\sigma)$ and $w(\varepsilon)$ indicate the

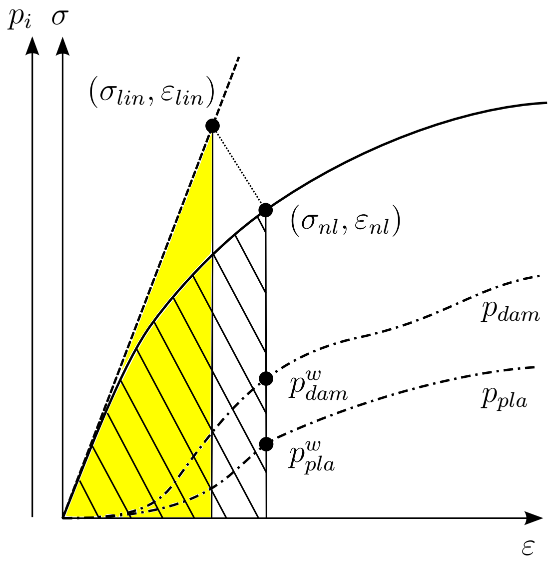

Figure 4.5: Mapping of linear and nonlinear states according to equal strain energy densities in the case of uniaxial loading. The yellow highlighted area below the linear response is equal to the hatched area below the unit cell response.

associated load path. If $p_i^{w(\sigma)} = p_i^{w(\varepsilon)}$ it may be assumed that the sensitivity of the energy fractions p_i regarding the loading history (i.e. different load paths) is negligibly small and the determined p_i^{σ} and p_i^{ε} may be interpreted as upper and lower estimates for the actual value of p_i whereas $p_i^{w(\sigma)}$ and $p_i^{w(\varepsilon)}$ may be interpreted as some other estimate for the actual value of p_i. It shall be noted that different values for p_i^{σ} and $p_i^{w(\sigma)}$ are just caused by the mapping procedure, while the evolution of the considered dissipated energy fraction is equal in both cases. The same consideration applies to p_i^{ε} and $p_i^{w(\varepsilon)}$. If $p_i^{w(\sigma)}$ and $p_i^{w(\varepsilon)}$ differ, the loading history, i.e. the shape of the load path (cf. Fig. 4.2 right), has recognizable influence on the evolution of the energy fractions and the application of the obtained results has to be done with special care since it is just assumed that radial stress and strain paths represent lower and upper estimates regarding the loading history influence. Hence, more critical (non-proportional) load paths may exist. Considering the application of the described methodology on structural components, it shall be stated that the presented approach cannot account for stress redistribution at the macroscopic length scale, i.e. in the component. As stated above the influence of non-proportional loading is accounted for in an approximate way at the length scale of the underlying unit cell computations (e.g. mesoscale), while the stress redistribution is just covered at the microscale. Hence, it can be stated that this approach is hardly applicable in the region of pronounced nonlinearities since the accompanied stress redistribution in the component is not covered. However, it is expected that reasonable predicitons of the dissipated energy fractions can be given in the slightly nonlinear regime thus extending the information on material exertion beyond the linear elastic limit.

4.2.2 Utilization of Generated Envelopes

After the completion of nonlinear unit cell simulations of a specified distribution of radial stress and strain paths, as described above, relevant data is stored in a database related to the material and microgeometry of the textile composite under consideration thus allowing for fast access of specific information. This database contains the homogenized stress and strain tensors and the corresponding dissipated energy fractions for each load path, hence, representing the basis for the proposed post-processing method. In the following, the different steps for applying the generated database on large-scale linear elastic analyses are outlined.

Input

In order to start with the post-processing routine, a linear elastic stress state $\underline{\boldsymbol{\sigma}}_{lin}$ of interest has to be chosen. The corresponding strain state $\underline{\boldsymbol{\varepsilon}}_{lin}$ is determined according to the already evaluated ABD matrix of the considered textile composite, cf. Eq. (4.2). For the further investigation the geometrical interpretation of $\underline{\boldsymbol{\sigma}}_{lin}$ and $\underline{\boldsymbol{\varepsilon}}_{lin}$ as vectors in plane stress and plane strain space, respectively, shall be used.

Find enclosing paths

Considering a mesh of radial paths in plane stress space, cf. Fig. 4.2, the first task in evaluating the properties of intermediate states is to find the computed sampling states which are closest to the specified one. Since the following procedure is equal for radial stress and strain paths it will just be discussed for radial stress paths. It can be stated that, if whole plane stress space is covered by a finite number of paths, several paths are found which enclose the input state $\underline{\boldsymbol{\sigma}}_{lin}$ in plane stress space, where the three tightest enclosing paths need to be determined in order to allow for a suitable interpolation of the actual state. In a first step, it is checked whether $\underline{\boldsymbol{\sigma}}_{lin}$ is parallel to one of the computed paths. In this case the determination of enclosing paths and the interpolation between different load paths is not required and the subsequent steps are just applied on the parallel path.

Therefore, the directional unit vectors $\underline{\boldsymbol{d}}^i$ and $\underline{\boldsymbol{d}}_{lin}$ of each computed path $\underline{\boldsymbol{\sigma}}^i$ and $\underline{\boldsymbol{\sigma}}_{lin}$ are evaluated and written in spherical coordinates, cf. Eq. (4.8), where θ denotes the azimuth angle and ϕ the elevation angle.

$$\underline{\boldsymbol{d}}^i = \begin{pmatrix} \theta^i \\ \phi^i \\ 1 \end{pmatrix}, \qquad \underline{\boldsymbol{d}}_{lin} = \begin{pmatrix} \theta_{lin} \\ \phi_{lin} \\ 1 \end{pmatrix} \tag{4.8}$$

Hence, if the condition in Eq. (4.9) is met the associated load path n is found to be parallel to $\underline{\boldsymbol{d}}_{lin}$ and the routine for finding enclosing paths is completed. Otherwise it is proceeded as follows.

$$\underline{\boldsymbol{d}}_{lin}^{T}\ \underline{\boldsymbol{d}}^{n} = 1 \tag{4.9}$$

Now, the orientation of each load path $\underline{\boldsymbol{d}}^{i}$ relative to $\underline{\boldsymbol{d}}_{lin}$ is evaluated by taking the difference of the azimuth and elevation components.

$$\theta_{rel}^{i} = \theta_{lin} - \theta^{i} \qquad \phi_{rel}^{i} = \phi_{lin} - \phi^{i} \tag{4.10}$$

The closest paths are then represented by small relative angles θ_{rel}^{i} and ϕ_{rel}^{i}. Therefore, a vector $\mathcal{D}^{i}$ containing the sum of the absolute values of θ_{rel}^{i} and ϕ_{rel}^{i} is introduced.

$$\mathcal{D}^{i} = |\theta_{rel}^{i}| + |\phi_{rel}^{i}| \tag{4.11}$$

The load paths related to the two smallest values in $\mathcal{D}^{i}$ are found to be the two closest paths to $\underline{\boldsymbol{d}}_{lin}$ and are denoted as $\underline{\boldsymbol{d}}_{encl}^{1}$ and $\underline{\boldsymbol{d}}_{encl}^{2}$. Since the third closest load path according to $\mathcal{D}^{i}$ is not necessarily the one so that the three chosen paths enclose $\underline{\boldsymbol{d}}_{lin}$ another criterion is introduced to ensure this property. It can be stated that three linearly independent directions $\underline{\boldsymbol{d}}^{i}$ form a basis in 3D vector space. Hence, if $\underline{\boldsymbol{d}}_{lin}$ can be represented by a linear combination of the chosen basis vectors so that just positive coefficients appear the basis is enclosing $\underline{\boldsymbol{d}}_{lin}$. In order to make sure that the closest suitable path is chosen for $\underline{\boldsymbol{d}}_{encl}^{3}$, the remaining load paths are sorted according to ascending values of $\mathcal{D}^{i}$ and consecutively proven if they satisfy the criterion in Eq. (4.12). The first of the remaining load paths satisfying this criterion is then chosen to be $\underline{\boldsymbol{d}}_{encl}^{3}$.

$$b_1\ \underline{\boldsymbol{d}}_{encl}^{1} + b_2\ \underline{\boldsymbol{d}}_{encl}^{2} + b_3\ \underline{\boldsymbol{d}}_{encl}^{3} = \underline{\boldsymbol{d}}_{lin}, \qquad b_1, b_2, b_3 \geq 0 \tag{4.12}$$

Interpolation of the actual state

Now, the mapping techniques for relating linear elastically computed states of a structural component to the nonlinear unit cell responses, as described in section 4.2.1, are applied on each of the enclosing paths. Again, for the sake of brevity just radial stress paths are considered since the procedure is equal for radial strain paths. Therefore, the norm of $||\underline{\boldsymbol{\sigma}}_{lin}||$, i.e. the length, is applied on each of the three paths thus marking three sampling stress states $\underline{\boldsymbol{\sigma}}^1_{encl}$, $\underline{\boldsymbol{\sigma}}^2_{encl}$ and $\underline{\boldsymbol{\sigma}}^3_{encl}$.

$$\underline{\boldsymbol{\sigma}}^i_{encl} = ||\underline{\boldsymbol{\sigma}}_{lin}||\ \underline{\boldsymbol{d}}^i_{encl} \qquad i = 1, 2, 3 \tag{4.13}$$

However, these sampling stress states will usually lie between computed stress states along the load path and the corresponding quantities, i.e. the energy fractions, are interpolated linearly regarding the lengths related to the neighbouring stress states, cf. Fig. 4.6, where the computed states are marked as $t-1$ and t. In the case of the equal strain energy mapping method, the sampling stress states are determined in a way such that they represent the state where w^{lin}_{tot} is reached. The interpolation between the computed states is then conducted regarding the

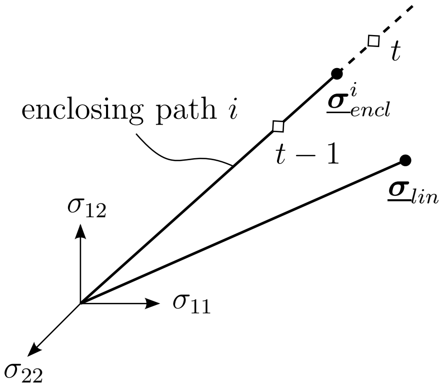

Figure 4.6: Interpolation of the state related to $\underline{\boldsymbol{\sigma}}^i_{encl}$ between the computed states at $t-1$ and t along the enclosing path i.

total strain energies of the neighbouring stress states. Now, a plane containing the three sampling states $\underline{\boldsymbol{\sigma}}^1_{encl}$, $\underline{\boldsymbol{\sigma}}^2_{encl}$ and $\underline{\boldsymbol{\sigma}}^3_{encl}$ is defined, cf. Eq. (4.14), where $\underline{\boldsymbol{n}}$ denotes the normal vector of the plane and $\underline{\boldsymbol{s}}$ represents the corresponding set of points.

$$\left(\underline{\boldsymbol{s}} - \underline{\boldsymbol{\sigma}}^1_{encl}\right)^T \ \underline{\boldsymbol{n}} = 0, \qquad \underline{\boldsymbol{n}} = \left(\underline{\boldsymbol{\sigma}}^2_{encl} - \underline{\boldsymbol{\sigma}}^1_{encl}\right) \times \left(\underline{\boldsymbol{\sigma}}^3_{encl} - \underline{\boldsymbol{\sigma}}^1_{encl}\right) \tag{4.14}$$

In order to determine the intersection of the input stress path with this plane, $\underline{\boldsymbol{\sigma}}_{lin}$ is defined as a line in plane stress space, cf. Eq. (4.15) left. By comparing the sets of points $\underline{\boldsymbol{s}}$ and $\underline{\boldsymbol{g}}$ the unknown coefficient ℓ is determined, cf. Eq. (4.15) right, and the intersection point $\underline{\boldsymbol{\sigma}}_{inter}$ is yield.

$$\underline{\boldsymbol{g}} = \ell \underline{\boldsymbol{d}}_{lin} \qquad \ell = \frac{\underline{\boldsymbol{\sigma}}^1_{encl} \cdot \underline{\boldsymbol{n}}}{\underline{\boldsymbol{d}}_{lin} \cdot \underline{\boldsymbol{n}}} \tag{4.15}$$

Finally, the quantities of interest, i.e. the dissipated energy fractions p, are evaluated using the inverse distance method, cf. Eq. (4.16), where the energy fraction corresponding to the input state is denoted as $p(\underline{\boldsymbol{\sigma}}_{lin})$ and p_k represents the energy fractions related to the sampling states. Fig. 4.7 illustrates this procedure.

$$p(\underline{\boldsymbol{\sigma}}_{lin}) = \sum_{k=1}^{3} \frac{v_k(\underline{\boldsymbol{\sigma}}_{inter})\ p_k}{\sum_{j=1}^{3} v_j(\underline{\boldsymbol{\sigma}}_{inter})} \qquad v_k(\underline{\boldsymbol{\sigma}}_{inter}) = \frac{1}{||\underline{\boldsymbol{\sigma}}_{inter} - \underline{\boldsymbol{\sigma}}^k_{encl}||^2} \tag{4.16}$$

Evolution of dissipated energy fractions

In order to allow for fast post-processing of structural components regarding occurring nonlinear mechanisms, the described procedure, together with the generated dataset, is implemented into Abaqus/Standard. Additionally, envelopes represent-

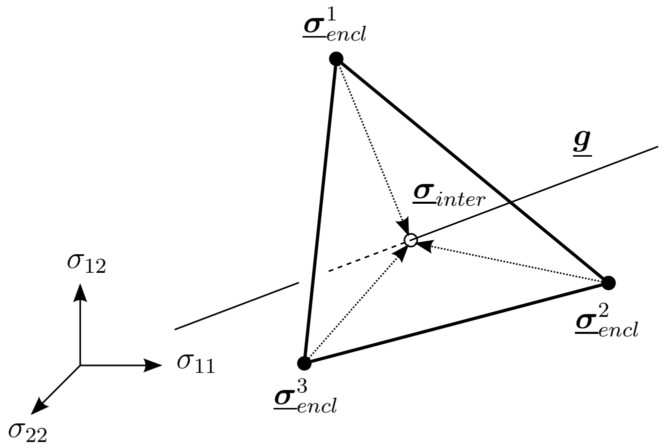

Figure 4.7: Intersection of the plane $(\underline{\boldsymbol{\sigma}}^1_{encl}, \underline{\boldsymbol{\sigma}}^2_{encl}, \underline{\boldsymbol{\sigma}}^3_{encl})$ with the line $\underline{\boldsymbol{g}}$. The distances between the corners and the intersection point $\underline{\boldsymbol{\sigma}}_{inter}$ are marked as dotted arrows.

ing the onset of the individual mechanisms are generated as surfaces in plane stress space where onset is related to a specified small (but nonzero) value of the corresponding dissipated energy fraction p_i. These initiation surfaces are then used to assess the occurring stress states by evaluating the intersection points with the respective stress paths and extracting the reserve and safety factors. Hence, a reserve factor > 1 indicates the onset of the considered mechanism and the corresponding stress state is interpreted as critical. Considering some structural component, these locations can easily be found by generating a contour plot of the reserve factor.

Now, critical stress states can be further investigated by passing them to the described post processing routine in order to get information about the nonlinear behaviour. Therefore, the enclosing paths are determined and the corresponding dissipated energy fractions p_i are evaluated. Since not only the current state but also the evolution of the occurring nonlinear mechanisms is of interest, the routine is executed for several proportional loading states up to a specified multiple of the investigated stress state. In this way, the sensitivity of the current state regarding further load increase can be estimated and an idea of the strength reserve of the component may be revealed. Although states with a reserve factor < 1 are not critical at the current state, their behaviour may deviate from the one of the investigated states upon further load increase and may lead to a more critical state than the investigated one. In order to incorporate this aspect in the assessment of stress states, additionally, a reserve/safety factor related to surfaces of higher values of p_i can be determined in the same way as described above thus allowing for a first examination of the evolution of p_i before selected states are investigated in detail.

Chapter 5

Applications

Within this chapter, the application of the proposed methodology shall be demonstrated in two steps. First, the generation of a material specific database and related energy dissipation envelopes is presented by the example of a 2/2 twill weave. Furthermore, the influence of different material models in terms of dissipated energies is outlined by comparing the responses of configurations featuring the elasto-brittle-damage model, cf. section 3.2.1, and the elasto-plasto-damage model, cf. section 3.2.2. In a second step, the usage of a generated database for assessing linear elastically computed stress states in large components regarding occurring nonlinearities shall be demonstrated by applying the proposed post-processing routine to a 4 point bending beam consisting of several layers of 30 degree twill braids.

All finite element simulations in the context of this work have been carried out using the commercial finite element code Abaqus/Standard v6.12/6.13, whereas the post-processing routine is based on a user defined subroutine and several Matlab scripts. The implementation in Abaqus is realized via the Abaqus GUI Toolkit.

5.1 2x2 Twill Weave

This section deals with the simulation of the nonlinear material behaviour in a 45 degree carbon/epoxy 2/2 twill weave based on an unit cell approach. In order to be able to assess arbitrary plane stress states, a distribution of some 200 radial stress and strain paths is simulated where all relevant results, such as the homogenized stress and strain tensors and the dissipated energy fractions p_i are stored in a database for use in combination with the proposed post-processing routine. Before the results are presented, the underlying finite element model describing the composite's mesostructure shall be summarized and the application of appropriate boundary conditions for simulating radial paths is explained.

5.1.1 Finite Element Model

Since some 200 nonlinear simulations are necessary in order to cover whole plane stress and strain space, a computationally efficient model is inevitable. Therefore, a shell element based unit cell approach modelling a representative volume element of the investigated composite is chosen. This model has been developed by Gager, cf. [11, 9] and is illustrated in Figs. 5.1 and 5.2. The mesostructure of the 2/2 twill weave is modelled by a piecewise linear ondulation of fibre tows with rectangular

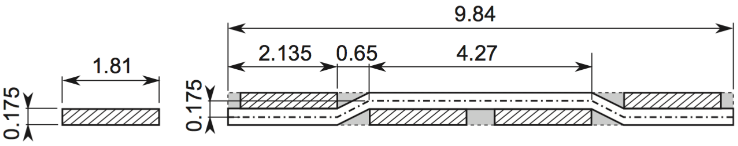

Figure 5.1: Cross section of the 2/2 Twill Weave showing the piecewise linear ondulation path and rectangular tow cross sections (hatched) with dimensions in mm. The dashed line represents the unit cell perimeter and the grey areas denote the matrix pockets [11].

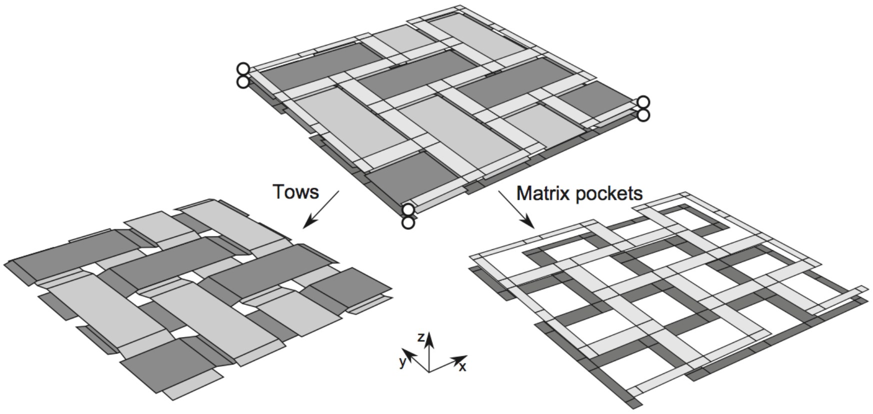

Figure 5.2: Shell element based unit cell separated into fibre tows and unreinforced matrix pockets. The white circles in the assembled configuration mark the unit cell's master nodes [11].

cross section, cf. Fig. 5.1. The unreinforced matrix pockets filling the hollow space between the tows consequently feature linearly varying thicknesses too. The unit cell's geometry is meshed using linearly interpolated, 4 noded shell elements with five section points in thickness direction, where the usual element size is 1/14th of the tow width. The reference planes of the tows and the matrix pockets shown in Fig. 5.2 are tied appropriately featuring perfect interfaces. Hence, delamination is not modelled. Furthermore, plane periodic boundary conditions, cf. section 3.1.1, are applied. For the following investigations, two configurations, A and B, of applied constitutive models, cf. section 3.2, are compared, as summarized in tab. 5.1.

Table 5.1: Applied constitutive models for capturing the behaviour of tows and matrix pockets.

	configuration A	configuration B
tows	elasto-brittle-damage	elasto-plasto-damage
matrix pockets	Drucker-Prager plasticity	elastic

Thus a computationally simpler model featuring an elasto-brittle-damage model for the tows and Drucker-Prager plasticity for the matrix pockets is confronted with a more sophisticated approach featuring an elasto-plasto-damage model for the tows and elastic matrix pockets.

Material data

The material parameters are chosen according to [8] and describe the material system Cycom977. The following tables give all necessary parameters to define the applied constitutive models. The sub- and superscripts follow the notation used in section 3.2. The parameters in tab. 5.4 are additionally needed to define the elasto-plasto-damage model, cf. section 3.2.2. These parameters comprise the slope and weakening parameters for the Puck criteria, the constants to define the power law plasticity models and other parameters which define the damage model and interaction of mechanisms. More information is given in [8].

Table 5.2: Initial engineering elastic constants, nominal strength values and specific fracture energies of the fibre tows. Values marked with $*$ are estimated. [8]

	E_l	$E_q = E_r$	$\nu_{lq} = \nu_{lr}$	ν_{qr}	
elastic	146 GPa	9 GPa	0.34*	0.61*	
constants	$G_{lq} = G_{lr}$	G_{qr}			
	4.27* GPa	2.8* GPa			
nominal	X^T	X^C	Y^T	Y^C	S
strengths	2100 MPa	1407 MPa	82 MPa	249 MPa	110* MPa
fract.	$G^{(ft)}$	$G^{(fc)}$	$G^{(mt)}$	$G^{(mc)}$	$G^{(ps)}$
energies	89.8 N/mm	78.3 N/mm	0.2 N/mm	0.8 N/mm	1.0 N/mm

Table 5.3: Parameters for viscous regularization. Values marked with $*$ are estimated. [8]

η^{ft}	η^{fc}	η^{mt}	η^{mc}
0.002^* s	0.002^* s	0.004^* s	0.004^* s

Table 5.4: Additional parameters needed to define the elasto-plasto-damage model for the fibre tows. [8]

Puck criterion	p^t	p^c	s	s	
	0.35	0.30	0.5 (1.0)	1.0	
power law plasticity	$\tilde{\sigma}_I$	k_I	n_I		
	22.8 MPa	161 MPa	0.214		
	$\tilde{\sigma}_{II}$	k_{II}	n_{II}		
	41.7 MPa	1175 MPa	0.364		
damage/ interaction	$e^{(f)}$	$e^{(m)}$	$k_d^{(m)}$	$\xi_{a(c)}^{(m)}$	μ_d
	0.01	0.01	8.00	0.015	0
	λ_I	λ_{II}	μ_I^t	μ_I^c	μ_{II}
	1.50	0.25	0.10	0.08	0.25

Table 5.5: Elastic properties of the matrix pockets and parameters for the Drucker-Prager plasticity model.

elastic const.	E	ν		
	3520 MPa	0.37		
Drucker-Prager	σ_y^t	β	ψ	K
	81.4 MPa	25°	25°	1

Tab. 5.5 summarizes the elastic properties of the unreinforced matrix pockets and gives the parameters to define the Drucker-Prager plasticity model which is applied in configuration A. It shall be noted that ideal plastic behaviour is assumed. Since $\beta = \psi$ associated flow is modelled in this case.

Boundary conditions

The application of boundary conditions is accomplished via the unit cell's master nodes, cf. Fig. 5.3, where also the $1, 2, 3$ coordinate system, on which the following considerations are based, is illustrated. In order to prevent rigid body motions, displacements of master nodes are restricted according to tab. 5.6. Furthermore, the displacements of SEB and SET are defined to be equal in 1 and 2 direction, as well as the ones of NWB and NWT in 2 direction, which suppresses the occurrence of global bending.

In order to apply boundary conditions corresponding to a radial stress path, as already done by Meindlhumer [20] for configuration A of this model, respective concentrated forces are assigned to the master nodes SEB and NWB. These are increased proportionally starting from a chosen initial increment thus resulting in a radial stress path. The relation between the concentrated forces and the stress state is given in section 3.1.2. For the simulation of radial strain paths, displacements corresponding to the desired strain state are assigned to SEB and NWB, cf. Eq. (3.9) and increased proportionally. It shall be noted that the

Table 5.6: Boundary conditions for preventing rigid body motions and coupling effects. Displacements in the stated directions are prescribed to be zero.

SWB	SWT	SEB	SET	NWB	NWT
$1, 2, 3$	$1, 2$	3	–	$1, 3$	–

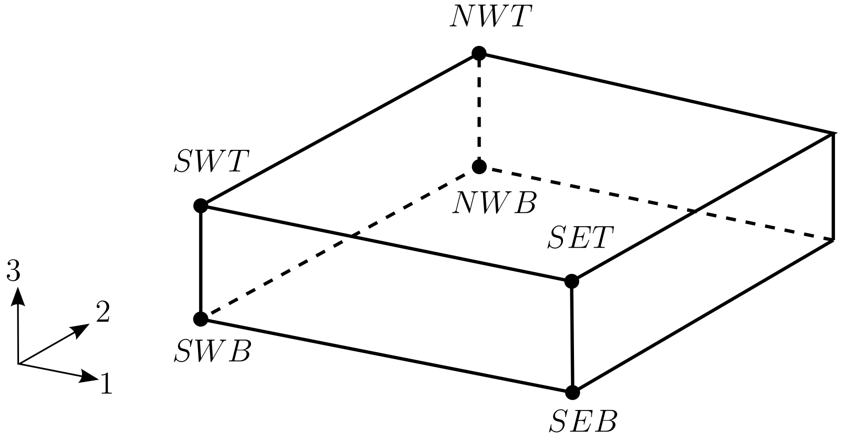

Figure 5.3: Illustration of the unit cell's master nodes. The $1, 2, 3$ coordinate system is aligned with the fibre tows, cf. [20]

presented boundary conditions model simple shear in both cases, although it would be possible to simulate pure shear in the case of radial strain paths.

Distribution of load paths

Up to this point, the simulation is set up for one specific stress or strain path, respectively. In order to generate a database for assessing arbitrary plane stress states, a distribution of load paths has to be selected. As stated in [20], the present weave exhibits several symmetries regarding loading in plane stress space. Thus, the response of the unit cell is assumed to be equal for positive or negative plane shear components σ_{12}, as well as for loading in 1 or 2 direction. The resulting symmetry planes in plane stress space are given in Eq. (5.1).

$$\sigma_{12} = 0 \qquad \sigma_{11} - \sigma_{22} = 0 \tag{5.1}$$

Since the results of Meindlhumer [20] have shown that a uniform distribution of radial stress paths does not give an optimum resolution for describing the evolution

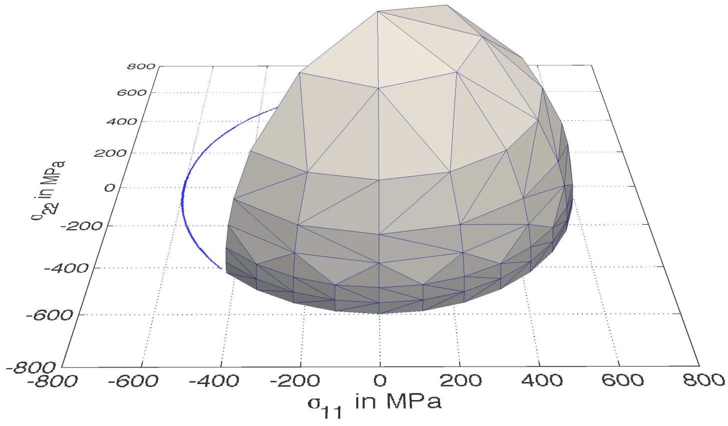

Figure 5.4: Computed distribution of radial stress paths illustrated in plane stress space. Existing symmetries are already utilized. Each node of the wireframe corresponds to one path. $s_{max} = 600$

of the investigated nonlinear mechanisms, an adapted distribution is chosen in this work, cf. Fig. 5.4. Therefore, more paths are computed in the region of small shear components σ_{12}, whereas a coarser distribution is chosen at higher values of σ_{12}. The coefficients determining the lengths of the radial stress and strain paths are chosen to be

$$s_{max} = 600 \qquad e_{max} = 0.02. \tag{5.2}$$

All results presented in the following are based on the distribution shown in Fig. 5.4, except the ones of configuration A for radial stress paths, which are taken from Meindlhumer [20].

5.1.2 Results

In the context of this work, computations based on the load path distribution shown in Fig. 5.4 have been conducted for radial strain paths of configuration A as well as for radial stress and strain paths of configuration B, cf. tab. 5.1. Thus, together with Meindlhumer's results [20], two entire datasets for both configurations have been generated. In the following, the differences between radial stress and strain paths shall be outlined before the influence of the applied constitutive model is investigated.

Comparison of radial stress and strain paths

In order to outline the difference in the unit cell's response regarding the considered load path, a comparison of stress-strain curves and the corresponding energy fractions is given in Fig. 5.5, where the cases of uniaxial tension and compression in tow direction are illustrated for both configurations A and B. The dashed lines represent radial stress paths, also indicated by the superscript σ, whereas solid lines mark radial strain paths, indicated by the superscript ε.

Considering the case of uniaxial tension, Fig. 5.5 (a) and (b), it can be stated that there is barely any noticeable difference between the responses for radial stress and strain paths of both configurations. Hence, it may be deduced that very little load history dependence, i.e. influence of the load path shape (cf. Fig. 4.2 right), is exhibited and energy fractions of related stress states may be considered as bounds in terms of the proposed post-processing routine. It shall be noted that the response of B showed very slow convergence at higher loads which is the reason for the smaller plot domain.

The case of uniaxial compression, Fig. 5.5 (b) and (d), shows good agreement between the load paths up to the slightly nonlinear regime. However, in the region of pronounced nonlinearity the responses start to deviate more and more. Furthermore, the assumption of upper and lower bounds for radial strain and stress paths is violated for both configurations, since the energy fraction corresponding to

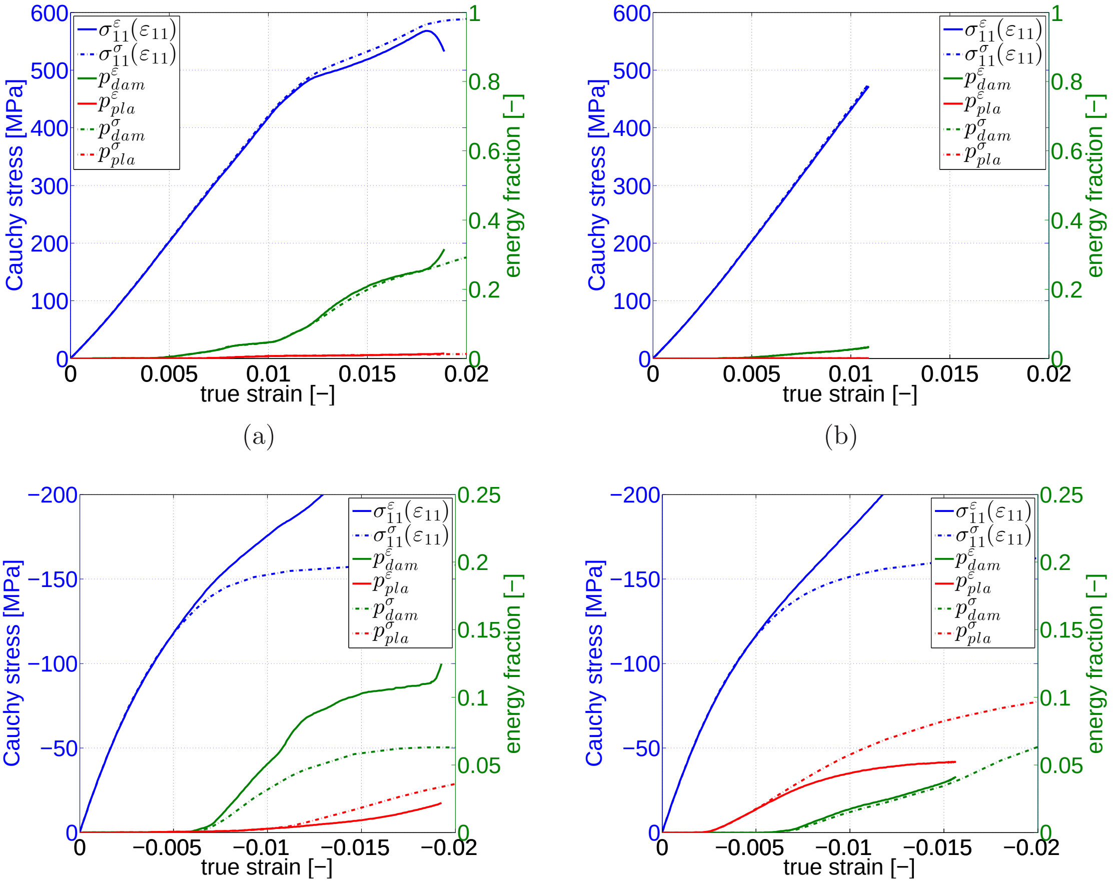

(a) (b)

(c) (d)

Figure 5.5: Stress-strain plots illustrating uniaxial tension, (a) and (b), and uniaxial compression, (c) and (d), of the unit cell. (a) and (c) correspond to configuration A whereas (b) and (d) represent configuration B. The results for radial stress paths of configuration A are taken from [20].

plasticity is always larger for radial stress paths $p_{pla}^{\sigma} > p_{pla}^{\varepsilon}$. Thus, the assumption of bounds cannot be maintained in this situation and the assessment of related stress states has to be done with special care. The responses may still represent bounds, although the underlying assumption is harmed, however, more critical paths are likely to exist. Obviously, the prescribed strains retard the propagation of plasticity, although they lead to higher stresses in loading direction. A reason might be the fact that the response corresponding to the radial strain path does not represent uniaxial loading in the nonlinear regime, cf. Eq. (4.2). Therefore, the assumption of bounds may be considered to be valid in cases where the responses of radial stress and strain paths show little deviation. For all other cases, higher or lower estimates of the energy fractions can't be assigned to radial stress or strain paths a priori, however, these distinct load paths may still represent upper and lower estimates. For the sake of completeness, it shall be noted, that the higher values of p^i_{pla} in configuration B are caused by the fact, that configuration A just accounts for plasticity in the matrix pockets whereas configuration B models plasticity in the fibre tows.

As already mentioned, stress and strain states corresponding to certain values of dissipated energy fractions p_i can be evaluated in order to form surfaces (envelopes) of constant values of p_i in stress and strain space. Naturally, envelopes corresponding to radial stress paths are described in plane stress space, whereas those corresponding to radial strain paths are described in plane strain space. A comparison of whole envelopes regarding load path influence would then require envelopes generated from radial strain paths to be described in plane stress space or vice versa, which is, however, no significant comparison since, for example, radial strain paths are curved in plane stress space and distances between the illustrated envelopes cannot be interpreted in terms of a proportional load factor, cf. Fig. 2.3.

The difference between the responses of radial stress and strain paths will be outlined once more when the application of the post-processing routine is discussed, cf. section 5.2.3. Nevertheless, surfaces corresponding to the onset of a nonlinear mechanism are equal for both paths since radial stress and strain paths are uniquely related in the linear regime.

Initiation envelopes

Based on the above statement, just initiation surfaces based on radial stress paths are presented where those corresponding to configuration A can be found in [20]. Envelopes marking the onset of damage and plasticity according to configuration B are illustrated in Fig. 5.6, where onset of an individual dissipative mechanism is defined as

$$p_i > 10^{-5}, \tag{5.3}$$

with p_i denoting the dissipated energy fraction of mechanism i, cf. Eq. (3.59). As can be seen, biaxial tension states ($\sigma_{11} > 0$, $\sigma_{22} > 0$) are more sensitive to damage since this mechanism is activated at lower stress states in this regime. For biaxial compression states, plasticity occurs first. Furthermore, there is a huge difference in the sensitivity to shear stresses. The initiation envelope corresponding

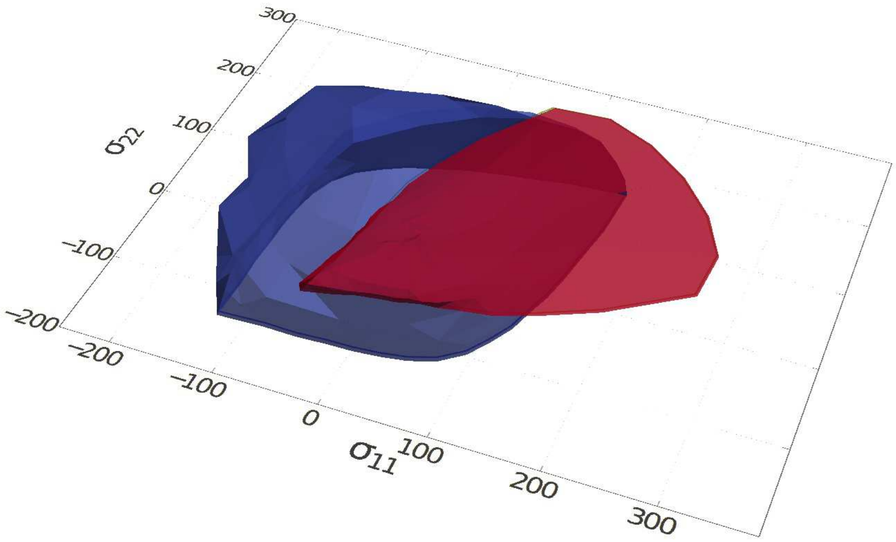

Figure 5.6: Surfaces marking the onset of damage (blue) and plasticity (red) in plane stress space according to configuration B. All values are in MPa.

to plasticity, cf. Fig. 5.6 (red), is rather flat meaning that already small shear stress components lead to the onset of plasticity whereas the onset of damage is located at much higher values of σ_{12}.

Comparison of material models

For the sake of brevity, the comparison of the influence of the applied constitutive models is conducted only for radial stress paths. Of course, the investigation could also be done for radial strain paths, which shall, however, be omitted in this case. In order to provide a suitable comparison of the evolution of damage and plasticity according to the two combinations of applied constitutive models, A and B, cuts along the symmetry planes of the corresponding envelopes, cf. Eq. (5.1), are presented in Figs. 5.7 and 5.8.

Considering the evolution of damage for biaxial stress states, cf. Fig. 5.7 (top), it can be seen that initiation occurs at equal stress states for both configurations. However, the propagation of damage takes place faster for configuration A, as the envelope for 2% damage almost coincides with the one for 1% damage of configuration B. Furthermore, it shall be noted that damage accumulates much faster at biaxial compression stress states for both configurations.

The evolution of damage in relation to the applied shear stress σ_{12}, as illustrated in Fig. 5.7 (bottom), shows quite different behaviour at all levels of p_{dam}. Thus, configuration A is much more sensitive to shear stress components than configuration B, where corresponding levels of p_{dam} are reached at approximately twice as high values of σ_{12}. Once damage has occurred, its propagation takes place rather fast for both configurations when the shear stress component is increased. The differences between configuration A and B in the presented damage envelopes

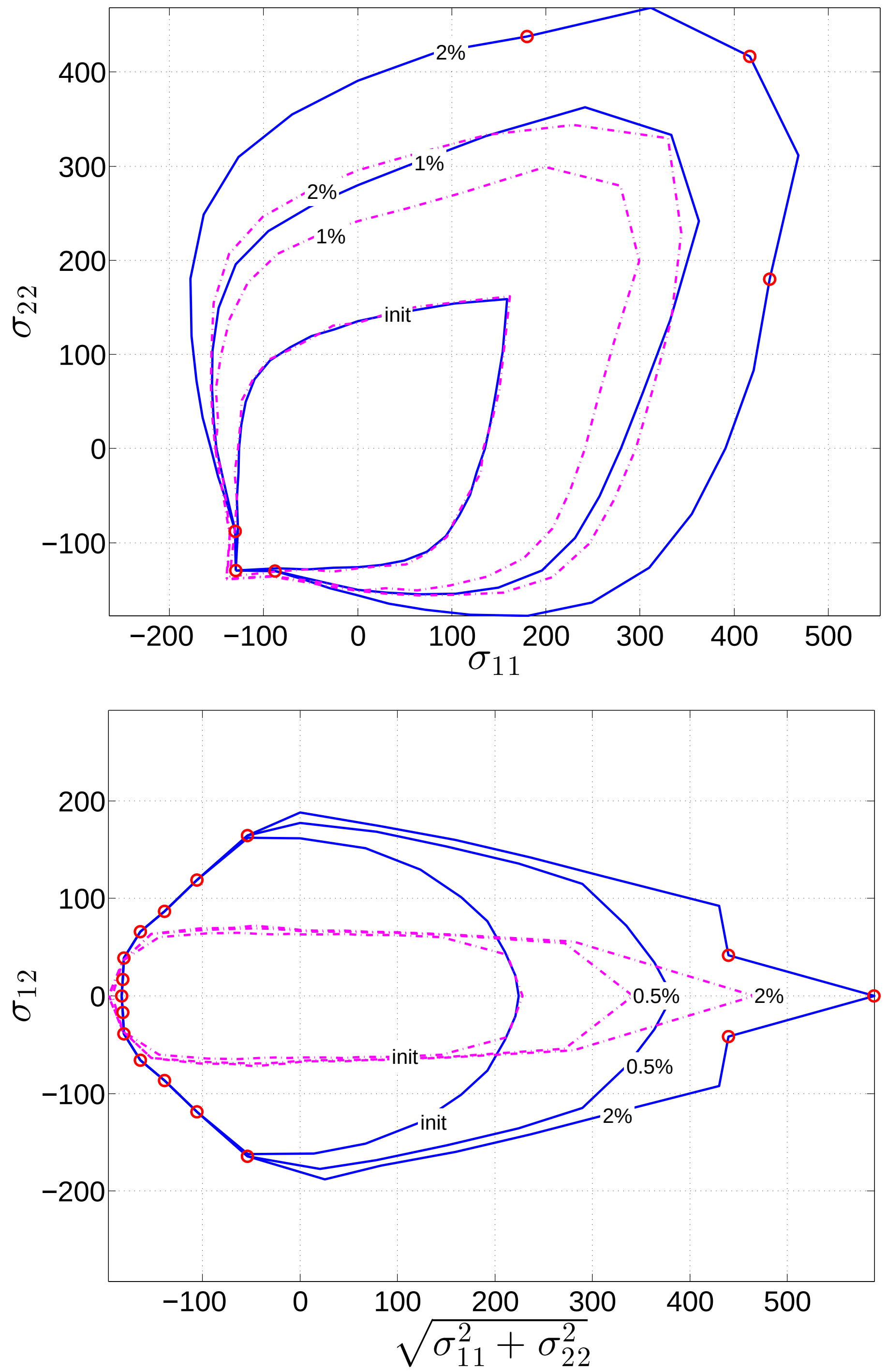

Figure 5.7: Evolution of damage in terms of p^{σ}_{dam} for configuration A (dashed lines) and configuration B (solid lines) in symmetry planes of plane stress space according to Eq. (5.1). Red circles mark points where the stated level of p^{σ}_{dam} has not been reached. All values are in MPa.

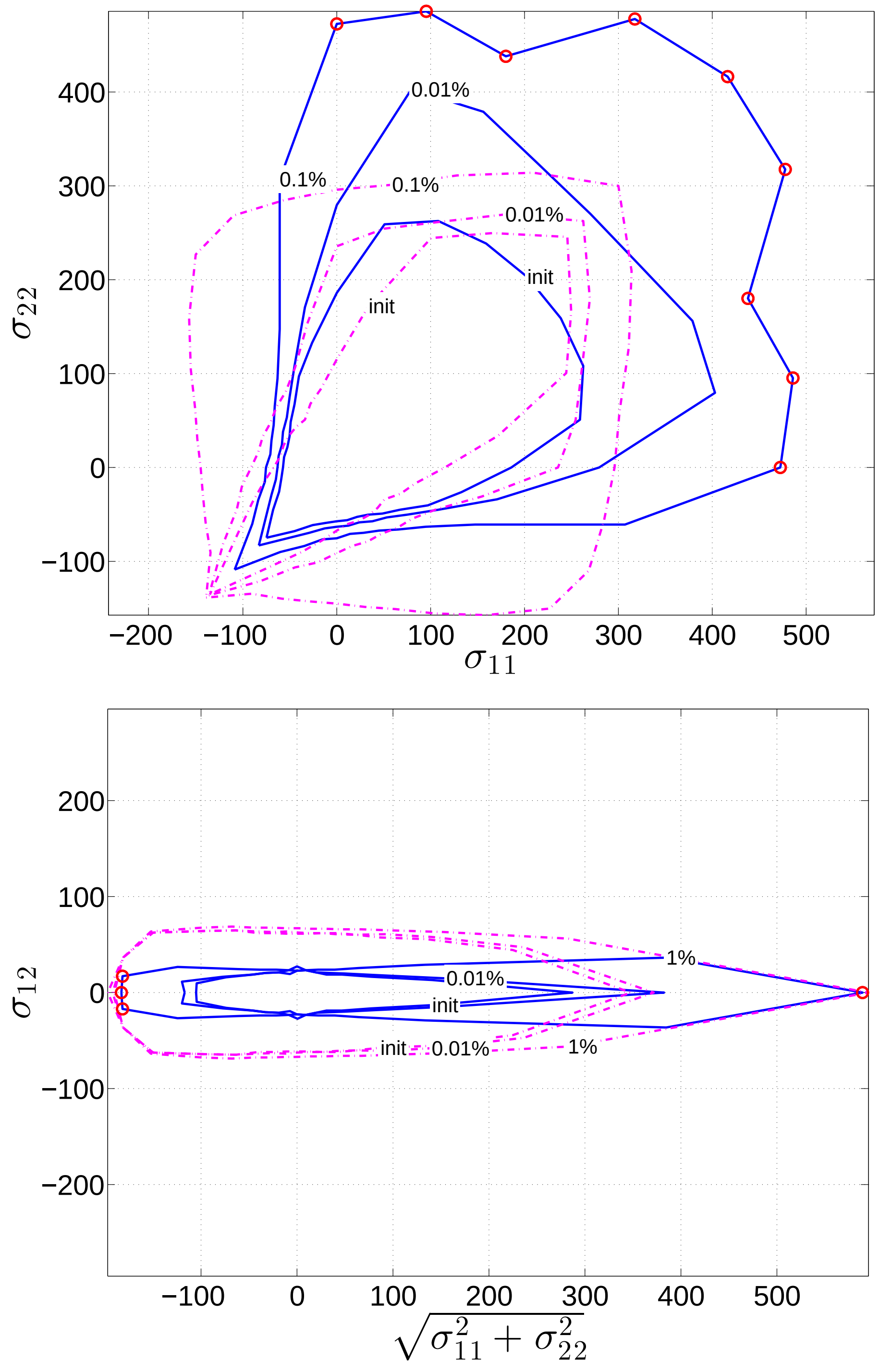

Figure 5.8: Evolution of plasticity in terms of p_{pla}^{σ} for configuration A (dashed lines) and configuration B (solid lines) in symmetry planes of plane stress space according to Eq. (5.1). Red circles mark points where the stated level of p_{pla}^{σ} has not been reached. All values are in MPa.

may be caused by the different approaches for modelling damage in the applied constitutive models, but, also the fact that configuration B accounts for plasticity in the tows is of influence. Comparing the evolution of plasticity, Fig. 5.8, it has to be kept in mind that configuration A just accounts for plasticity in the matrix pockets whereas configuration B just accounts for plasticity in the tows. Hence, envelopes representing the same value of p_{pla} have quite different shapes. Considering biaxial stress states, cf. Fig. 5.8 (top), it can be stated that plasticity propagates faster for tensile stress states ($\sigma_{11} > 0,\ \sigma_{22} > 0$) in configuration A, whereas at compressive stress states the propagation takes place faster in configuration B. Considering the stress states where the illustrated levels of p_{pla} are reached in comparison with the ones for p_{dam}, it can be stated that plasticity plays a minor role in the tensile region for both configurations, whereas, especially for configuration B, its influence is of more importance at compressive stress states. Both configurations are quite sensitive to shear stress components, however, configuration B is especially sensitive to pure shear loading. Combining the predictions of both configurations, it can be stated that plasticity is induced in the tows at earlier stages than in the matrix pockets, whenever shear stress components are present. The red circle in Figs. 5.7 and 5.8 mark points where the stated level of p^{σ}_{pla} has not been reached.

In order to investigate the dominance of damage and plasticity regarding different stress paths, i.e. different directions in plane stress space, the dissipated energy fraction due to damage, p_{dam}, is considered at a certain level of p_{pla} and vice versa. Therefore, stress and strain paths corresponding to the symmetry planes stated in Eq. (5.1) are investigated, where the energy fractions are evaluated as follows.

$$\begin{aligned} p^{i}_{dam} &= p^{i}_{dam}(p^{i}_{pla} = 0.01) = p^{i}_{dam}(p^{i,0.01}_{pla}) \qquad i \in \{\sigma,\ \varepsilon\} \\ p^{i}_{pla} &= p^{i}_{pla}(p^{i}_{dam} = 0.01) = p^{i}_{pla}(p^{i,0.01}_{dam}) \qquad i \in \{\sigma,\ \varepsilon\} \end{aligned} \tag{5.4}$$

Hence, p_{dam} is evaluated at the load increment where p_{pla} reaches a level of 1% and vice versa for each considered load path. The superscript i in Eq. (5.4) denotes whether radial stress or strain paths are considered. The evaluation of the described procedure is illustrated in Fig. 5.9 for both configurations A and B, where the load path 1 always corresponds to states with

$$\sigma_{11} = \sigma_{22} \qquad \sigma_{11},\ \sigma_{22} < 0, \tag{5.5}$$

whereas the last load path in each plot in Fig. 5.9 represents states with

$$\sigma_{11} = \sigma_{22} \qquad \sigma_{11},\ \sigma_{22} > 0. \tag{5.6}$$

Thus, Figs. 5.9 (a) and (b) correspond to paths where the ratio between σ_{11} and σ_{22} is varied while Figs. 5.9 (c) and (d) illustrate the variation of σ_{12} for states with $\sigma_{11} = \sigma_{22}$, where just positive values of σ_{12} are considered.

First, the occurrence of damage and plasticity shall be discussed for biaxial stress states ($\sigma_{12} = 0$), cf. Fig. 5.9 (a) for configuration A and Fig. 5.9 (b) for configuration B. It can be seen that plasticity in the matrix pockets plays a minor role at these loading scenarios since the damage fraction at 1% plasticity is always reasonably higher than 1%, cf. Fig. 5.9 (a). The largest influence of damage occurs at uniaxial tension in tow direction. The situation for configuration B is quite different, since both mechanisms seem to be equally important according to Fig. 5.9 (b), where tow plasticity is dominant for compressive states with a peak in the region of uniaxial compression in tow direction and damage is dominant for tensile states. Again, the largest influence of damage can be observed at uniaxial tension in tow direction. Considering the influence of shear components on the dominance of the occurring mechanisms it can be stated that damage and plasticity

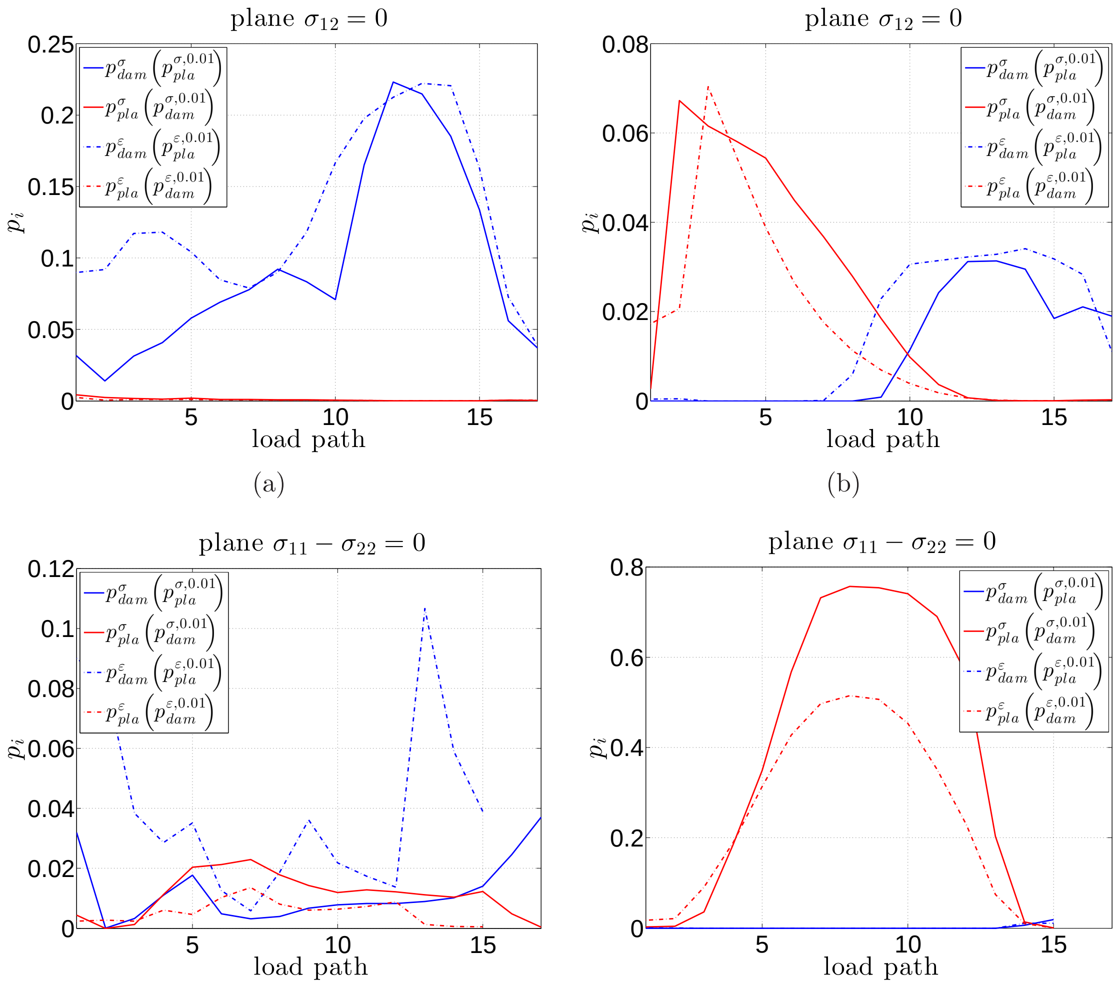

(a) (b) (c) (d)

Figure 5.9: Illustration of the dominance of damage and plasticity regarding different load paths, i.e. directions in plane stress space, cf. Eq. (5.4). (a) and (c) represent configuration A whereas (b) and (d) represent configuration B.

in the matrix pockets are equally important in configuration A, cf. Fig. 5.9 (c), where the region in the middle of the plot corresponds to plane shear and the first and last load path represent states without shear component. Taking a look at the same situation for configuration B reveals that tow plasticity is highly dominant for increasing shear stress components while damage has almost no influence in comparison. Thus, combining the predictions of both configurations it can be stated that plasticity in the matrix pockets has just minor impact on the overall dissipated energy fractions. Whenever compressive states or states with nonzero shear components are considered, tow plasticity plays a dominant role and should therefore not be neglected in these situations. Furthermore, it has been observed that radial strain paths qualitatively give a higher amount of damage but lead to less plasticity in comparison to radial stress paths for both configurations. It shall be noted, that points in Figs. 5.7 and 5.8 where the stated level of an energy fraction has not been reached are caused by the dominance of another mechanism. Thus, for example, high damage fractions are not reached for compressive states with nonzero shear components since tow plasticity is dominant in this region.

5.2 Structural Application

Now, the procedure for utilizing a generated dataset in order to assess occurring nonlinearities in large structural components based on linear elastic finite element simulations shall be presented by the example of a U-section beam with variable flange height in a four point bending test set-up consisting of four layers of biaxial ±30° braidings. Therefore, in a first step a dataset capturing the nonlinear behaviour of the considered material system is generated by conducting unit cell simulations as described before, which is then integrated in the proposed post processing routine in order to determine and assess critical locations in the U-section beam. First, the unit cell model and some differences to the one presented in the former section are described. Afterwards, the model of the beam is summarized and the loading situation is investigated.

5.2.1 Unit Cell Model

The finite element model for investigating the mesoscale structure of a single layer of the ±30° twill braiding is quite similar to the one described in section 5.1. Of course, the angle between the fibre tows is different and additionally, the tows are modelled with lenticular cross section and a smooth ondulation path, thus, featuring a more realistic geometry. An illustration of the modelled geometry is given in Fig. 5.10. This model has also been developed by Gager [11, 9], where more details on the modelling strategy are found.

Since the braid geometry indicates that tow plasticity is going to be an essential mechanism, the elasto-plasto-damage model, cf. section 3.2.2, is chosen to simulate the tow behaviour while the matrix pockets are modelled by linear elastic constitutive relations. This configuration is expected to be suited to the investigated loading conditions, as outlined in the former section.

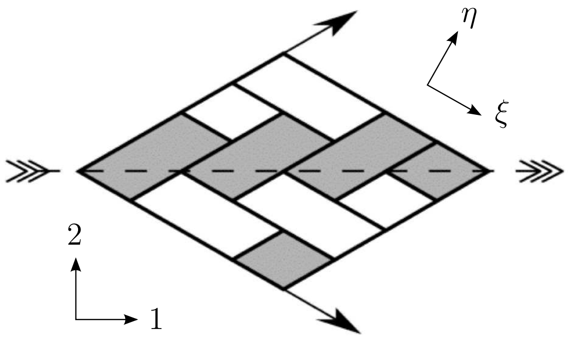

Figure 5.10: Geometry of the ±30° twill braiding with indicated periodicity vectors, cf. [9]. The $1, 2$ coordinate system is denoted as braid coordinate system and is used to describe the orientation of the braid on a macroscopic component. The ξ, η coordiante system is aligned with one tow direction and represents the unit cell coordinate system.

Material data

The considered braid features a RTM6/HTS40 matrix/fibre system. The material properties and additional parameters needed to define the constitutive models are presented in the tabs. 5.7, 5.8, 5.9 and 5.10, where the sub- and superscripts follow the notation used in section 3.2.

Boundary conditions

The boundary conditions are applied in a similar way as for the twill weave unit cell and the same nomenclature as illustrated in Fig. 5.3 is used. The locked master node displacements are stated in tab. 5.11, where the unit cell coordinate system ξ, η, ζ is utilized. Its axes are rotated through $\alpha = -30^\circ$ to the braid coordinate system such that ξ is aligned with a tow direction, cf. Fig. 5.10. The

Table 5.7: Initial engineering elastic constants, nominal strength values and specific fracture energies of the fibre tows. [9]

	E_l	$E_q = E_r$	$\nu_{lq} = \nu_{lr}$	ν_{qr}	
elastic	203.165 GPa	11.988 GPa	0.22	0.6785	
constants	$G_{lq} = G_{lr}$	G_{qr}			
	5.611 GPa	3.571 GPa			
nominal	X^T	X^C	Y^T	Y^C	S
strengths	2791 MPa	1400 MPa	33 MPa	175 MPa	76.4 MPa
fract.	$G^{(ft)}$	$G^{(fc)}$	$G^{(mt)}$	$G^{(mc)}$	$G^{(ps)}$
energies	89.8 N/mm	78.3 N/mm	0.2 N/mm	0.76 N/mm	1.0 N/mm

Table 5.8: Additional parameters needed to define the elasto-plasto-damage model for the fibre tows. [9]

Puck criterion	p^t	p^c	s	s	
	0.35	0.30	1.0	1.0	
power law plasticity	$\tilde{\sigma}_I$	k_I	n_I		
	20.7 MPa	171.6 MPa	0.229		
	$\tilde{\sigma}_{II}$	k_{II}	n_{II}		
	37.12 MPa	1390.8 MPa	0.3895		
damage/ interaction	$e^{(f)}$	$e^{(m)}$	$k_d^{(m)}$	$\xi_{a(c)}^{(m)}$	μ_d
	0.01	0.01	8.00	0.015	0
	λ_I	λ_{II}	μ_I^t	μ_I^c	μ_{II}
	1.50	0.25	0.10	0.08	0.25

Table 5.9: Elastic properties of the matrix pockets. [9]

E	ν
2890 MPa	0.38

Table 5.10: Parameters for viscous regularization. [9]

η^{ft}	η^{fc}	η^{mt}	η^{mc}
0.002 s	0.002 s	0.004 s	0.004 s

Table 5.11: Boundary conditions for preventing rigid body motions and coupling effects. Displacements in the stated directions are prescribed to be zero. The ξ, η, ζ coordinate system is aligned such that the ξ axis is parallel with a tow direction, cf. Fig 5.10.

SWB	SWT	SEB	SET	NWB	NWT
ξ, η, ζ	ξ, η	η, ζ	η	ζ	$-$

transformationn relation between the two coordiante system follows as

$$\begin{pmatrix} x_\xi \\ x_\eta \end{pmatrix} = \begin{pmatrix} \cos\ \alpha & \sin\ \alpha \\ -\sin\ \alpha & \cos\ \alpha \end{pmatrix} \begin{pmatrix} x_1 \\ x_2 \end{pmatrix} \tag{5.7}$$

Additionally, the displacements of NWB and NWT are defined to be equal in 1 and 2 direction as well as the displacements of SEB and SET in 1 direction in order to suppress global bending. Concentrated forces or displacements, respectively, for simulating radial stress and strain paths are prescribed to the master nodes SEB and NWB in a similar way as described for the twill weave unit cell. Again, simple shear is modelled.

Distribution of load paths

The load path distribution for generating the dataset for the post processing routine is equal to the one illustrated in Fig. 5.4, however, the ±30° braiding shows just symmetric behaviour about the plane

$$\sigma_{12} = 0. \tag{5.8}$$

Hence, a hemisphere in plane stress space has to be simulated instead of the quarter sphere in Fig. 5.4. The coefficients s_{max} and e_{max} determining the lengths of the computed stress paths and strain paths are chosen to be

$$s_{max} = 800 \qquad e_{max} = 0.03. \tag{5.9}$$

5.2.2 U-section Beam Model

The finite element model of the U-section beam with variable flange height in a four point bending test set-up illustrated in Fig. 5.11 has been developed by Salcher [30]. The beam is modelled using shell elements with an average edge lentgh of 1/24 of the beam height h, where existing symmetries at $\ell/2$ and $w/2$ are utilized. The connection of the half cylinder, the plate and the beam is modelled via surface to surface contact and the application of the load F is handled through a distinct node which is coupled to all others of the half cylinder in order to simulate a realistic test set-up. The plates between the steel cylinders and the beam are assumed to consist of aluminium and ensure that the concentrated load is distributed at the region of load application. The beam is supported at two cross sections, between

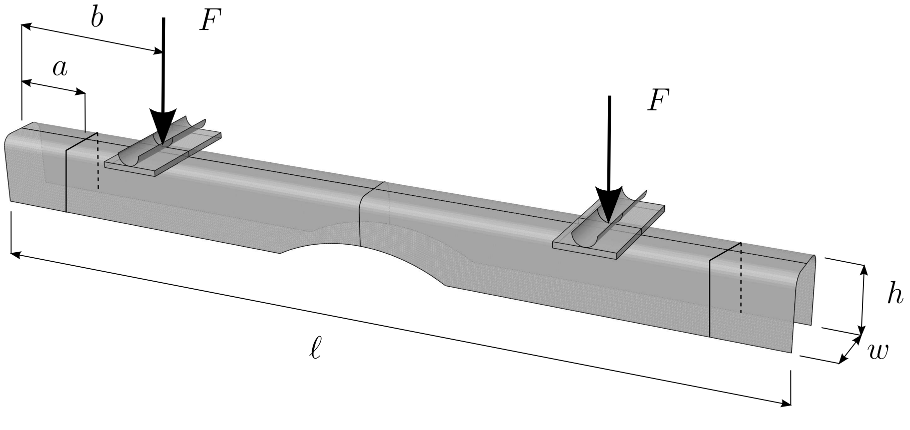

Figure 5.11: Isometric view of the investigated four point bending beam with the applied load F. ℓ = 700mm, w = 50mm, h = 60mm, a = 50 mm, b = 150 mm. The marked cross sections indicate the locations of supports. The braiding is aligned such that the 1-axis of the braid coordinate system is parallel to the length direction and the 2-axis lies in the plane of the beam surface, cf. Fig 5.10.

Table 5.12: Effective material data applied to each layer of the investigated beam. The transverse shear moduli ($*$) are estimated. Coordinate 1 is parallel to the length direction of the beam and 3 is always normal to the surface. 2 denotes the transverse in plane direction.

E_1	E_2	ν_{12}	G_{12}	G_{13}^*	G_{23}^*
42569 MPa	8717.8 MPa	1.5123	24140 MPa	24140 MPa	2890 MPa

the left border and the left load application and between the right border and the right load application, where the applied load F is

$$F = 200 \text{ N}. \tag{5.10}$$

The beam itself consists of four layers of ±30° twill braidings, where effective material properties are applied to each layer, cf. tab. 5.12. The $1, 2, 3$ cooridnate system according to tab. 5.12 is aligned in parallel to the braid coordinate system illustrated in Fig. 5.10. The braidings are applied such that the 1-axis of the braid coordinate system is aligned with the length axis of the beam and the 2-axis lies in the plane of the beam surface, cf. Fig. 5.10. The effective material properties are evaluated based on the unit cell model presented above and correspond to the initial stiffness of four layers stacked in-phase [9]. Although these properties do not correspond to the ones used for generating the database of nonlinear unit cell responses, where just a single layer is considered, this practice is used due to the fact that single layer properties underestimate the stiffness of stacked layers since they do not account for the interaction between adjacent layers. Furthermore, the case that a component is made out of a single layer of some braiding is rather unusual. The dissipated energy fractions are assumed to be just slightly depending on the number of layers considered and therefore the combination is considered to be reasonable.

5.2.3 Macroscopic Results - Assessment of Nonlinearities

Now, a linear elastic simulation of the presented four point bending beam is conducted while, already at this stage, a user subroutine is implemented into Abaqus, which accesses envelopes marking the onset of damage and plasticity. These envelopes are evaluated from the generated dataset according to the onset condition Eq. (5.3) and delivered as VTK file.

This user subroutine represents the first step in the post processing procedure since it evaluates a reserve factor corresponding to the utilized envelopes for each mechanism regarding proportional load increase and provides the respective factor as an output variable directly selectable in the Abaqus Viewer. This way, a fast overview of critical locations on the structure is given. However, it shall be noted that the locations found this way may not be the only critical spots in the structure as stated in section 4.2.2.

Fig. 5.12 shows the reserve factors related to damage and plasticity as contour plots for the most critical layer. The critical spots are found to be in the region of $\ell/2$ along the length direction of the beam, where damage has not occurred up to the current state, as can be seen in Fig. 5.12 (a) which illustrates the region of the highest occurring reserve factor for damage initiation. The most critical spot regarding plasticity is found to be the lower edge at $\ell/2$, cf. Fig. 5.12 (b), where a reserve factor of two indicates that plastic deformations have already occurred in this region. The green area in the vicinity of this spot exhibits a reserve factor of about one and indicates the border of the domain where plasticity may appear. The other layers do not exhibit as high reserve factors and the corresponding plots are therefore not shown. Up to this point no information about the nonlinear response at the critical spots has been given and it has just been stated that plasticity is supposed to occur at the discussed locations. In order to gain knowledge of the extent of plasticity at these locations and to estimate the sensitivity of certain locations regarding further load increase the dataset containing all computed nonlinear unit cell responses is utilized, cf. section 4.2, and a functionality to directly select a certain element and pass the stress state over to the post processing routine is implemented into Abaqus via the Abaqus GUI Toolkit. Thus, all locations of interest can easily be selected and investigated regarding the evolution of damage and plasticity. First, the state exhibiting a reserve factor of $RF_{pla} = 2$ regarding plasticity shall be investigated, cf. Fig. 5.12 (b). The post processing routine has shown that the this state does not exhibit damage initiation up to a

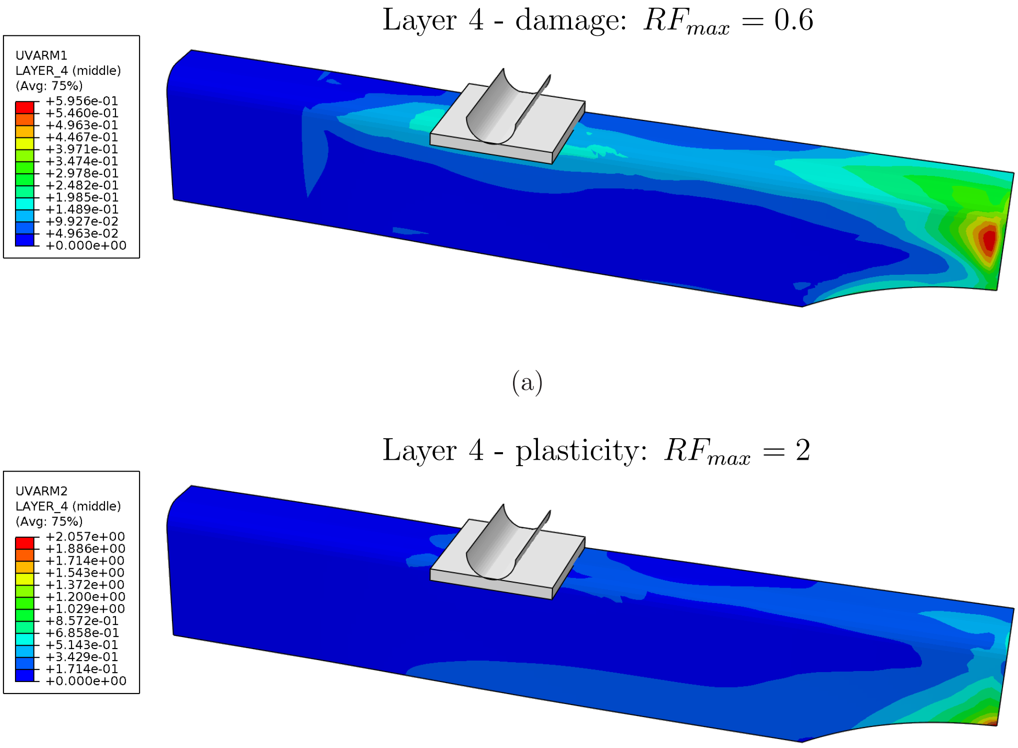
Layer 4 - damage: $RF_{max} = 0.6$

(a)

Layer 4 - plasticity: $RF_{max} = 2$

(b)

Figure 5.12: Contour plots of reserve factors for the most critical layer. The red regions mark the specified maximum value of the reserve factor RF_{max}. Layers are counted from bottom to top, hence, layer 4 denotes the top layer.

proportional load increase by a factor of two and, hence, a plot illustrating the evolution of damage is not given for this state. The evolution of plasticity in terms of proportional load increase is shown in Fig. 5.13. As can be seen, the plasticity fractions corresponding to radial stress and strain paths, p^{σ}_{pla} and p^{ε}_{pla}, mark some upper and lower estimates thus indicating a value between 2.5% and 4% for the actual plasticity fraction p_{pla} at the current state. The energy based plasticity fractions $p^{W(\sigma)}_{pla}$ and $p^{W(\varepsilon)}_{pla}$, cf. section 4.2.1, are coincident up to the current state but start to deviate upon further load increase. Hence, it can be stated that the loading history influence is of minor importance at the considered state and it may be assumed that the plasticity fractions p^{σ}_{pla} and p^{ε}_{pla} represent upper and lower bounds on the actual value of p_{pla}. At further load increase the plasticity fraction is steadily growing and reaches an upper estimate of 16% at a load fraction of two. Additionally, the load fraction where the initiation criterion for p_{pla}, cf. Eq. (5.3), has been met is marked with a circle in Fig. 5.13 and can be identified with a value of 0.4, which corresponds to the evaluated reserve factor of about two in Fig. 5.12 (b). Furthermore it can be seen that the value p_{pla} stays quite low in

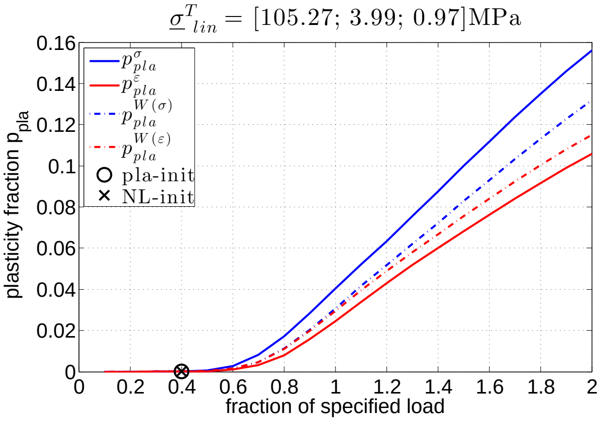

Figure 5.13: Evolution of the plasticity fraction p_{pla} in terms of proportional load increase at the critical location illustrated in Fig. 5.12 (b). The specified stress state $\underline{\boldsymbol{\sigma}}_{lin}$ denotes the stress components according to Voigt notation and is based on the braid coordinate system, cf. Fig. 5.10.

the region between onset of plasticity and a load fraction of 0.6 thus giving rise to the assumption that a safety factor regarding plasticity onset may be reduced in such situations. Of course, such an approach has to be verified by accompanying experiments.

Now, the location where the highest reserve factor regarding damage occurs, cf. Fig. 5.12 (a), shall be investigated regarding the sensitivity to further load increase. The contour plots in Fig. 5.12 reveal that, additionally to the reserve factor of $RF_{dam} = 0.6$ for damage onset, the reserve factor for plasticity onset is close to one in this region. Hence, the proposed post processing routine shall give information on the evolution of damage and plasticity at this location, as illustrated in Fig. 5.14 for the damage and plasticity fractions, p_{dam} and p_{pla}, in terms of proportional load increase. It can be seen that the initiation criterion for plasticity is met at a load fraction of 1.1 whereas damage onset is observed at a load fraction of 1.3. Again, the energy fractions corresponding to radial stress paths, p_i^σ,

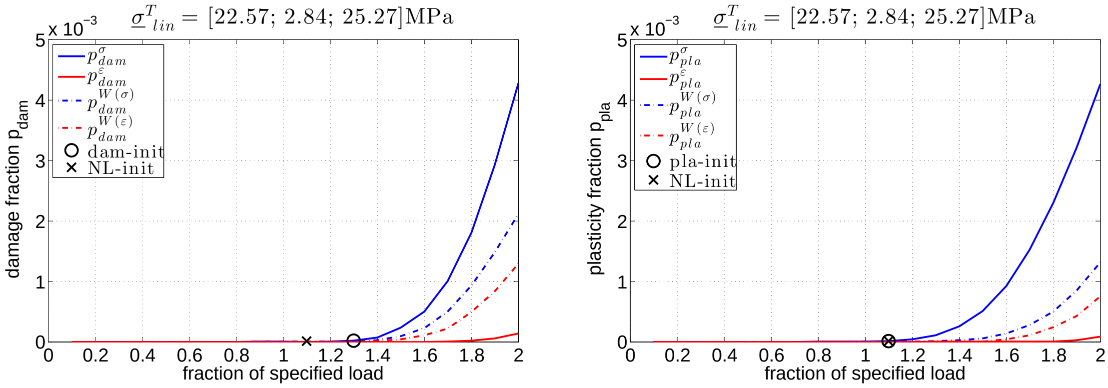

(a) (b)

Figure 5.14: Evolution of the damage fraction p_{dam} (a) and the plasticity fraction p_{pla} (b) in terms of proportional load increase at the location of the highest damage reserve factor, cf. Fig. 5.12 (a). The specified stress state $\underline{\boldsymbol{\sigma}}_{lin}$ denotes the stress components according to Voigt notation and is based on the braid coordinate system, cf. Fig. 5.10.

represent upper estimates whereas the ones corresponding to radial strain paths, p_i^ε represent lower estimates on the actual values of p_i. It shall be noted that, contrary to the situation in Fig. 5.13, the damage and plasticity fractions based on the equivalent strain energy mapping procedure, $p_{pla}^{W(\sigma)}$ and $p_{pla}^{W(\varepsilon)}$, already deviate just after the onset of the considered mechanism thus indicating that loading history influence is not negligible even in the slightly nonlinear region. Hence, predictions of the amount of damage and plasticity at increased loads have to be interpreted with great care since there may be load paths leading to more critical states than the ones predicted for radial stress and strain paths. In this case, information on the actual loading history should be taken into account in order to estimate the validity of the underlying assumptions of the proposed methodology. The current state according to Fig. 5.14 may be interpreted to be just moderately sensitive to load increase since, even at a load fraction of two, the upper estimates for p_{dam} and p_{pla} reach values of about 0.4%, which are considerably small compared to the current amount of plasticity ($\approx 3\%$) at the location investigated before. However, damage fractions p_{dam} may need to be treated different compared to the ones for plasticity, p_{pla}, since certain amounts of either fractions have not been investigated regarding structural failure. Hence, critical values of p_{dam} and p_{pla} cannot be stated within the scope of this work but can may be determined in combination with experiments.

It shall be noted that the presented approach cannot account for stress redistribution at macroscopic length scales, i.e. in the component. However, the influence of non-proportional loading is captured in an approximate way at the mesoscale while stress redistribution is just accounted for at the microscale. Therefore, reasonable results may just be expected as long as the loading state of the considered component stays in the slightly nonlinear regime.

Chapter 6

Conclusion

The application of fibre reinforced composites (FRCs) increases significantly in almost every field of engineering, not least due to their favourable weight specific properties as high specific stiffness and strength. In order to fully exploit their potential, it is necessary to reliably predict the nonlinear structural response of components consisting of FRCs. However, the coverage of all relevant nonlinear mechanisms in large structural analyses leads to vast computational demands and is therefore, in practice, hardly feasible. In order to resolve this disadvantage, a two step methodology is proposed which extends the predictional capabilities of large-scale linear elastic analyses by combining them with information on nonlinear effects gained through unit cell analyses and thus reduces the computational effort to a practicable extent. Since this combination is meant to be entirely decoupled, effects like stress redistribution cannot be accounted for on the macroscopic scale, i.e. in the component. Nevertheless, it is assumed that the influence of non-proportional loading is captured in an approximate way in terms of upper and lower estimates given by the simulation of related radial stress and strain paths. Of course, this approxiamtion is just valid at the length scale of the underlying unit cell computations, e.g. the mesoscale. Now, unit cell responses of a sufficient number of paths representing plane stress states are computed while dissipated energies are monitored in order to characterize and quantify occurring nonlinearities. This information is then stored in a material specific database and represents the basis of the proposed methodology. In a second step, arbitrary plane stress states occurring at some chosen locations in linear elastic structural analyses are mapped to corresponding states of the generated database thus facilitating the assessment of material nonlinearities on the macroscale. Hence, once a dataset has been generated the assessment of arbitrary linear elastic stress states can be done within seconds independently from the investigated structure.

The application of this methodology is demonstrated on the basis of two different textile composites, a twill weave and a ±30° twill braiding, where the mapping procedure is applied on a linear elastically computed U-section beam with variable flange height in a four point bending test set-up. It is shown that the unit cell responses corresponding to radial stress and strain paths deviate clearly recognizable in the region of pronounced nonlinearities, indicating non negligible influence of the loading history in terms of non-proportional loading. Furthermore, the assumption of upper and lower estimates related to radial strain and stress paths is found to be reversed in some situations. Hence, estimates on the dissipated energy fractions have to be treated with special care whenever the above conditions are observed since more critical load paths are likely to exist. However, the responses for radial stress and strain paths tend to coincide in the slightly nonlinear region thus allowing the predicted energy fractions to be interpreted as upper and lower estimates. In some cases the energy fractions stay relatively low after the corresponding onset criterion has been met whereas they are increasing considerably fast in other situations. Observations like this give rise to the assumption that some loading situations may be less critical than others and the presented approach may be directly utilized for adapting safety factors in component design, of course, after an experimental validation of the proposed methodology has been conducted. Finally, it shall be noted that the energy dissipation monitoring concept is not restricted to the application on textile composites and can be universally applied whenever the investigated mechanisms can be tracked by their dissipated energies.

In order to allow a reasonable application of the proposed methodology in component design, critical levels of dissipated energy fractions have to be identified by accompanying experiments. Such information would extend the predictional capabilities regarding strength reserve. The disadvantage of the decoupled procedure is represented by the inability to account for stress redistribution at the macroscopic scale. Hence, the generated dataset may be utilized directly coupled with large scale simulations instead of its application at the post-processing stage in order to overcome this shortcoming. However, such an approach still contains the assumption of radial paths.

Bibliography

[1] H. Altenbach. *Kontinuumsmechanik*. Springer-Verlag Berlin Heidelberg, 2012.

[2] A. Anthoine. Derivation of the in-plane elastic characteristics of masonry through homogenization theory. *Int. J. Solids and Structures*, 32(2):137–163, 1995.

[3] H. J. Böhm. *A Short Introduction to Basic Aspects of Continuum Micromechanics*. Institute of Lightweight Design and Structural Biomechanics, Vienna University of Technology, 2013.

[4] F. C. Campbell. *Manufacturing Processes for Advanced Composites*. Elsevier Advanced Technology, 2004.

[5] Dassault Systemes Simulia Corp., Providence, RI, USA. *Abaqus/Standard User's Manual, Version 6.12*.

[6] T. Daxner and F. Rammerstorfer. *Nichtlineare Finite Elemente Methoden*. Institute of Lightweight Design and Structural Biomechanics, Vienna University of Technology, 2012.

[7] A. DeSimone, J.-J. Marigo, and L. Teresi. A damage mechanics approach to stress softening and its application to rubber. *Eur. J. Mech. A/Solids*, 20:873–892, 2001.

[8] T. Flatscher. *A Constitutive Model for the Elasto-Plasto-Damage Ply Bahviour in Laminated FRP Composites: Its Developement, Implementation and Application in FEM Simulations.* PhD thesis, Institute of Lightweight Design and Structural Biomechanics, Vienna University of Technology, 2010.

[9] J. Gager. *Modeling and Simulation Concepts for Advanced Braided Composites.* PhD thesis, Vienna University of Technology, Institute of Lightweight Design and Structural Biomechanics, 2013.

[10] J. Gager, M. Meindlhumer, M. Schwab, and H. E. Pettermann. Numerically predicted damage and failure envelopes of composites featuring nonlinear material behaviour. In *The 19th International Conference on Composite Materials*, 2013.

[11] J. Gager and H. Pettermann. Numerical homogenization of textile composites based on shell element discretization. *Composites Science and Technology*, 72:806–812, 2012.

[12] Z. Hashin. Failure criteria for unidirectional fiber composites. *Journal of Applied Mechanics*, 47:329–334, 1980.

[13] R. Hill. The elastic behaviour of a crystalline aggregate. *Proc.Phys.Soc.London*, A65:349–354, 1952.

[14] M. Hinton, A. Kaddour, and P. Soden, editors. *Failure Criteria in Fibre Reinforced Polymer Composites: The World-Wide Failure Exercise.* Elsevier Ltd., 2004.

[15] J. Hult and F. G. Rammerstorfer. *Engineering Mechanics of Fibre Reinforced Polymers and Composite Structures.* Springer-Verlag Wien New York, 1994.

[16] R. M. Jones. *Mechanics of Composite Materials.* Taylor and Francis, 1999.

[17] M. Knops. *Analysis of failure in fiber polymer laminates.* Springer-Verlag Berlin Heidelberg New York, 2008.

[18] I. Lapczyk and J. A. Hurtado. Progressive damage modeling in fiber-reinforced materials. *Composites Part A*, 38:2333–2341, 2007.

[19] C. Marte. Untersuchung von 2/2-Twill-Gewebe Laminate mit Hilfe von 3D-Finite Elemente Einheitszellen. Master's thesis, Institute of Lightweight Design and Structural Biomechanics, Vienna University of Technology, 2004.

[20] M. Meindlhumer. Schädigungs- und Versagensvorhersage von Gewebelaminaten durch mechanismenbasierte Hüllflächen. Master's thesis, Institute of Lightweight Design and Structural Biomechanics, Vienna University of Technology, 2013.

[21] J. Michel, H. Moulinec, and P. Suquet. Effective properties of composite materials with periodic microstructure: a computational approach. *Comput. Methods Appl. Engrg.*, 172:109–143, 1999.

[22] T. Nelson. *787 Systems and Performance.* Boeing, 2005.

[23] D. H. Pahr. *Experimental and Numerical Investigations of Perforated FRP-Laminates.* PhD thesis, Institute of Lightweight Design and Structural Biomechanics, Vienna University of Technology, 2003.

[24] V. Prasad. http://theflyingengineer.files.wordpress.com/2011/11/l.jpg.

[25] A. Puck. *Festigkeitsanalyse von Faser-Matrix-Laminaten.* Carl Hanser Verlag Muenchen Wien, 1996.

[26] A. Puck and H. Schürmann. Failure analysis of FRP laminates by means of physically based phenomenological models. *Computers Science an Technology*, 58:1045–1067, 1998.

[27] A. Puck and H. Schürmann. Failure analysis of FRP laminates by means of physically based phenomenological models. *Computers Science an Technology*, 62:1633–1662, 2002.

[28] J. Rabotnov. *Creep Problems in Structural Members*, volume 7 of *North-Holland series in Applied Mathematics and Mechanics*. North-Holland, Amsterdam, Netherlands, 1969.

[29] A. Reuss. Berechnung der Fließgrenze von Mischkristallen auf Grund der Plastizitätsbedingung für Einkristalle. *ZAMM*, 9:49–58, 1929.

[30] A. Salcher. FEM-Auslegung einer Kohlefaser-Geflechtstruktur. (to be submitted). Master's thesis, Vienna University of Technology, Institute of Lightweight Design and Structural Biomechanics, 2013.

[31] C. Schuecker and H. E. Pettermann. A continuum damage model for fiber reinforced laminates based on ply failure mechanisms. *Compos. Struct.*, 76(1-2):162–173, 2006.

[32] H. Schürmann. *Konstruieren mit Faser-Kunstdtoff-Verbunden.* Springer-Verlag Berlin Heidelberg New York, 2007.

[33] I. Skrna-Jakl. *Leichtbau mit faserverstärkten Werkstoffen. Lecture notes.* Institute of Lightweight Design and Structural Biomechanics, Vienna University of Technology, 2011.

[34] W. Voigt. Über die Beziehung zwischen den beiden Elasticitäts-Constanten isotroper Körper. *Ann.Phys.*, 38:573–587, 1889.